Air Force Institute of Technology

AFIT Scholar

3-2020

Determination and Simulation of the Neutron Spectrum of Nuclear Detonations and Surrogate Sources

Taylor M. Nichols

Follow this and additional works at: https://scholar.afit.edu/etd

Part of the Nuclear Engineering Commons

Determination and Simulation of the Neutron
Spectrum of Nuclear Detonations and Surrogate
Sources

THESIS

Taylor M. Nichols, Ctr., USAF

AFIT-ENP-MS-20-M-109

DEPARTMENT OF THE AIR FORCE
AIR UNIVERSITY

AIR FORCE INSTITUTE OF TECHNOLOGY

Wright-Patterson Air Force Base, Ohio

AFIT-ENP-MS-20-M-109

DETERMINATION AND SIMULATION OF THE NEUTRON SPECTRUM OF

NUCLEAR DETONATIONS AND SURROGATE SOURCES

THESIS

Presented to the Faculty

Department of Nuclear Engineering

Graduate School of Engineering and Management

Air Force Institute of Technology

Air University

Air Education and Training Command

in Partial Fulfillment of the Requirements for the

Degree of Master of Science in Nuclear Engineering

Taylor M. Nichols, B.S.

Ctr., USAF

March 2020

AFIT-ENP-MS-20-M-109

DETERMINATION AND SIMULATION OF THE NEUTRON SPECTRUM OF

NUCLEAR DETONATIONS AND SURROGATE SOURCES

THESIS

Taylor M. Nichols, B.S.
Ctr., USAF

Committee Membership:

Dr. John W. McClory
Chair

LTC Michael B. Shattan
Member

Dr. Justin A. Clinton
Member

AFIT-ENP-MS-20-M-109

Abstract

This research determined a methodology for characterizing the Fast Beam Facility (FBF) at The Ohio State University Nuclear Reactor Laboratory to test the response of photovoltaic arrays to nuclear weapon radiation. Additionally, this research developed neutron and gamma nuclear weapon output spectra of two environments for comparison to the FBF spectrum. A Bonner sphere spectrometer (BSS), coupled with the unfolding program Maximum Entropy Deconvolution (MAXED), was employed as a means of determining the energy spectrum of neutrons. Using the ISO 8529 americium beryllium (AmBe) source as the a priori default spectrum, MAXED was used to unfold the spectrum of neutrons detected using the BSS from a 500 mCi AmBe source. An MCNP model of the experiment was created with the ISO 8529 spectrum used as the neutron source spectrum. The resulting unfolded neutron spectrum has similar characteristics to the ISO 8529 reference spectrum, with peaks located at 3.1 and 4.7 MeV corresponding to the peaks of the reference spectrum. Spectral deviations from the ISO 8529 reference spectrum caused by low-energy, non-neutron interaction events or neutrons thermalized through interactions in the experimental environment are accounted for in the model and reflected in the final unfolded neutron spectrum. Next, the neutron and gamma flux received at a fixed photovoltaic array from two detonation scenarios were modeled with MCNP6: a ground-only and a single building model for various height-of-bursts and yields. Thermalization due to neutron interaction and scattering of gamma rays with environmental materials is observed in the spectrum of resulting radiation incident on the photovoltaic array.

Acknowledgements

"Most people say that it is the intellect which makes a great scientist. They are wrong: it is character." - Albert Einstein

I would like to thank my partner and family for supporting me through this process. I would also like to thank Dr. McClory, Major Bevins, and the staff at The Ohio State University Nuclear Research Lab for their time and support involving the research conducted for this thesis.

Taylor M. Nichols

Table of Contents

List of Figures

List of Tables

DETERMINATION AND SIMULATION OF THE NEUTRON SPECTRUM OF NUCLEAR DETONATIONS AND SURROGATE SOURCES

I. Introduction

With international relations changing rapidly over the last half-decade, it is never too soon to examine the capabilities of other technology that can help in detecting, measuring, and defining weapon detonations. North Korea's recent weapon detonations are prime examples of the situations where this technology would be the most useful, as quickly identifying a detonation will provide information on how to defend against such weapons. Retired U.S. Army Gen. Vincent Brooks said in a press-conference, "Nuclear or not ... these are missiles that do threaten our two most important allies and our principal allies in northeast Asia. . . This has to be something that the United States is drawn into addressing," [1]. This is especially true when considering the growing tensions originating from Russia increasing its nuclear forces, China's pursuit of new nuclear capabilities, and threats to the U.S. and its allies by North Korea [2]. Nonetheless, Thomas Cartledge, a nuclear engineer with the Defense Threat Reduction Agency (DTRA), stated that "The scenario has changed. . . Now, if you see a mushroom cloud go off in New York City, you won't know who did it, or what kind of weapon they used," [3]. This issue still persists even with the changes to the international relations of the United States.

1.1 Motivation and Purpose

Photovoltaic (solar) panels are one of the technologies that potentially meets the capabilities described above. According to Dr. Lei Raymond Cao of The Ohio State University Department of Mechanical and Aerospace Engineering, "a pre-coded solar charge controller or power management system could capture the time sequence of signature from the detonation, sending real-time information to a central control center" [4]. Solar panels in the vicinity of a blast could collect and send characteristic information of a nuclear blast to an information center outside of the damage zone, providing real-time data.

In order to further examine the capability of photovoltaics as a form of nuclear detection, the response of the panels must be examined using a nuclear weapon like source of radiation. Since it is not an option to use an actual nuclear weapon (NW) to observe the effects on the panels, a surrogate source must be used and manipulated to mimic the radiation output by a NW detonation. The source planned for this research is the Fast Beam Facility (FBF) at The Ohio State University Nuclear Research Lab (OSU-NRL). The FBF was characterized previously near the core of the reactor using bare wire activation with the programs STAYSL and SAND-II. As shown in Figure 1, the neutron spectrum inside the FBF ranges from 0.01 eV to 10 MeV. Although there will be differences in the neutron spectra from this region near the core and the region at the end port of the FBF, this spectrum provides insight into the energies of the neutrons emitted by the reactor. By shaping this spectrum, the FBF will be a useful neutron source that can be used to mimic nuclear weapon output spectra.
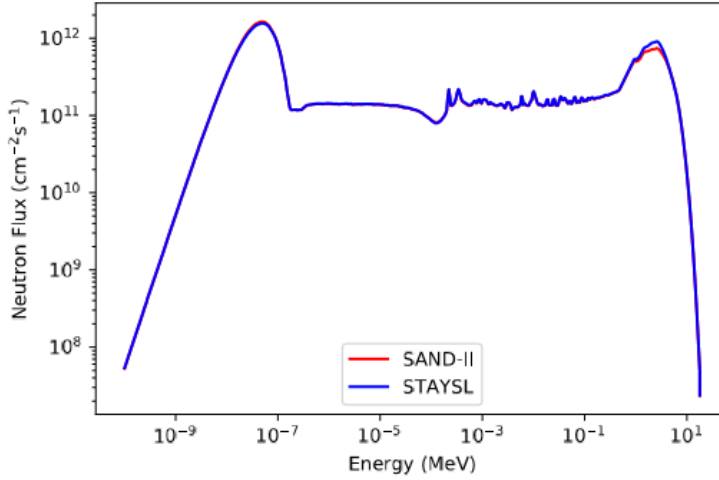
Figure 1. The neutron energy spectrum of the Fast Beam Facility at OSU NRL.

To accomplish the task of shaping the beam from the reactor, a neutron collimator will be attached to the end of the beam port amongst other filters, as shown in Figure 2 [4]. The neutrons will pass through the collimator and filters and interact with a solar cell. A beam chopper placed between the end of the neutron beam port and the solar cell along with a timing signal from a control-aquisition instrument will allow for time modulation of the beam. Additionally, a xenon flash lamp and another timing signal will simulate sunlight for combined light and neutron exposure. For experimental consistency, the solar cell and xenon flash lamp will both be in a light-tight enclosure to minimize background light interference. Lastly, a beam stop will be placed behind the solar cell to ensure the safety of the experiment. This setup will allow the effects of the radiation on the solar cell to be recorded and studied in future research.
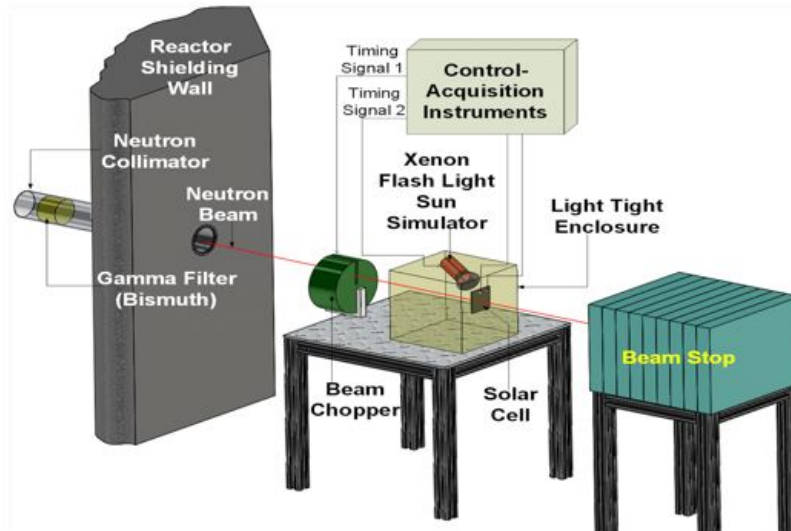
Figure 2. Schematic drawing of real-time data acquisition with a time modulated fast neutron beam for combined light and neutron exposure. Reproduced with permission from [4].

The purpose of the research conducted for this thesis is to determine a methodology for characterizing the Fast Beam Facility (FBF) at The Ohio State University Nuclear Reactor Laboratory. After characterization, the FBF can then be utilized to test the response of photovoltaic arrays to nuclear weapon radiation. The flux wire activation used to characterize the neutron spectrum near the core will not be used to characterize the FBF due to energy limitations. Flux wires utilize threshold reactions that are typically on the order of a few MeV. This does not give the discrimination necessary to characterize the FBF. The Bonner sphere spectrometer, however, produces a continuous response up to approximately 12 MeV [5]. For this reason, the capabilities of the Bonner sphere spectrometer is examined. This entails testing the accuracy of the Bonner sphere spectrometer (BSS) using a source with a known neutron spectrum. Furthermore, the Maximum Entropy Deconvolution (MAXED) program is used to unfold the neutron spectrum of the known source. This research will also examine the viability of MAXED in producing accurate unfolded neutron spectra. Lastly, this research also provides modeled weapon output spectra for vari-

4

ous yields and height-of-bursts using the Monte-Carlo N-Particle (MCNP) transport program. The weapon output neutron spectrum can be compared to the Fast Beam Facility neutron spectrum so that modifications can be made to the port. The goal is to shape the neutron beam coming from the port so that it is characteristically similar to that of a nuclear weapon output spectrum. This additional work will be conducted outside of the scope of this thesis by the OSU-NRL and AFIT staff and researchers.

1.2 Methods and Limitations

Using the publicly released neutron and gamma output spectra of Fat Man, an MCNP input file is created to calculate the neutron and gamma fluence one kilometer away from a detonation. This models the NW detonation spectra that is most likely to interact with a solar panel placed approximately 1 km from a blast. The spectra are shown in Figure 3 and Figure 4. The spectra 1 km from the source provides a good initial guess as to what energy photons and neutrons will interact with the solar panel in a realistic scenario. Thus, these spectra are referenced when comparing the output neutron spectrum from the FBF. Before characterizing the FBF at OSU, the BSS is tested for accuracy using a source with a known spectrum. In this research, the source is an americium-beryllium (AmBe) source. MCNP and MAXED are the two programs utilized to do the spectrum unfolding. Using the latest version of MCNP (MCNP6), the response functions of the BSS are modeled for various neutron energies. Then, the input data, response function, and an *a priori* spectrum are used by MAXED to deconvolve the measured neutron spectrum of the AmBe source. More details on this process is included in a later chapter.
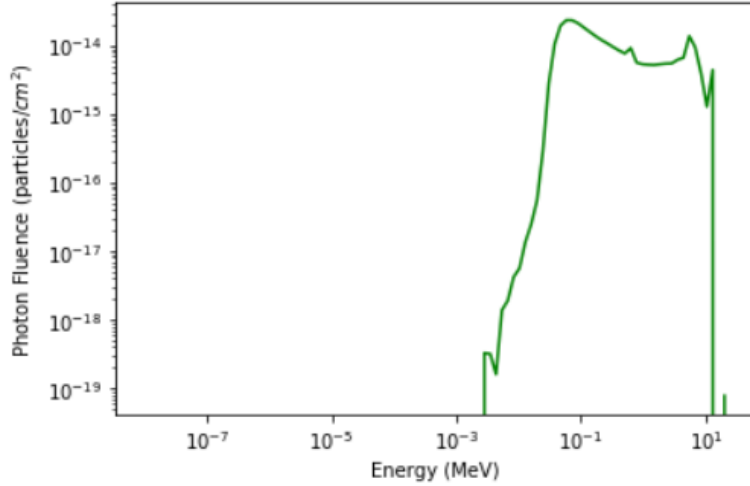
Figure 3. The photon energy spectrum 1 km from a source modeled after Fat Man.
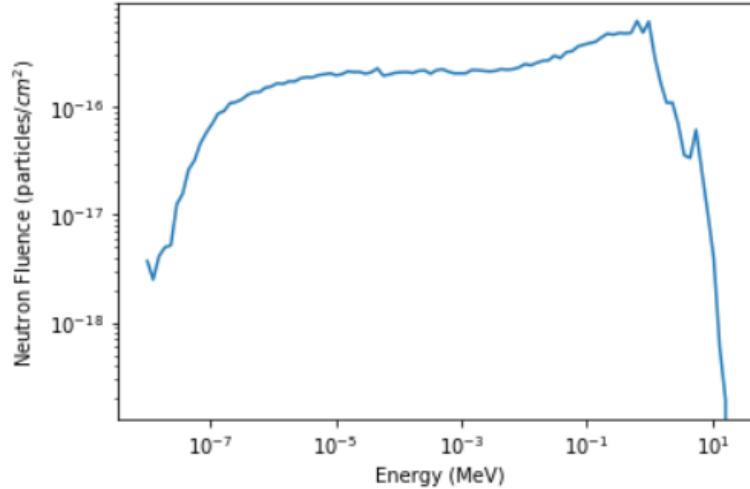
Figure 4. The neutron energy spectrum 1 km from a source modeled after Fat man.

There are a few limitations to this research that will be noted here. First, a large portion of this work is computational which comes with limitations of its own. One of the most notable limitations is the statistical uncertainty associated with most Monte-Carlo based programs. Another limitation is the fitting method used by MAXED. By requiring an *a priori* spectrum, MAXED leans heavily on the competence of the user. Additionally, a higher quality *a priori* spectrum leads to improved MAXED spectral responses. This is not much of a challenge for neutron sources that have

6

well-known and documented spectra, however it is much more challenging for neutron spectra that have not yet been characterized. Lastly, a limitation that touches on the theoretical side of this research involves the NW spectrum model. The model is based on Fat Man which may or may not be an accurate representation of modern nuclear weapons. Because of this, the nuclear weapon spectrum might be slightly different than the spectrum that would be emitted if a nuclear detonation occurred today.

The portion of this work that is experimental also has limitations. The BSS, although it has a wide range continuous response, is limited by the number of polyethylene spheres. The number of spheres correlates to the energy discrimination of the system. More spheres of varying sizes would allow for more discrimination between neutron energies, however it also increases the complexity of the unfolding process which can lead to inaccurate unfolding. This is due to the response matrix of the detector and its associated polyethylene spheres: when the response functions for spheres overlap, or when the functions are very similar, unfolding programs cannot discriminate between the neutrons collected by the different spheres. This means that although the energy of the neutron may vary slightly, the neutrons collected by two spheres with similar responses will be unfolded and assigned to approximately the same energy. Additionally, BSS's are known for their low energy resolution due large fluctuations in the number of collisions the neutrons undergo before being detected as well as indistinguishable capture reactions [6]. Another limitation is the source used to test the accuracy of the BSS. The americium beryllium (AmBe) source emits a broad energy range of neutrons: up to approximately 11 MeV, where the average neutron energy is approximately 4 MeV. For this reason, it is a good source to test the versatility of the BSS. However, it is slightly different than the modelled FBF neutron spectrum in that it has a higher flux for the lower energies, whereas the FBF is expected to have a higher flux for the faster neutrons.

II. Theory

The concepts and theory involved in the research are discussed in the following sections. This includes literature related to the topics described in the previous chapter.

2.1 Radiation Interactions

In order to better understand the underlying physics of neutron interactions after they emerge from the nuclear weapon, various concepts must first be discussed. These concepts include the fundamental theories behind neutron interactions. By understanding the interactions of neutrons in the environment after they emerge from the weapon, the resulting spectra that reaches the photovoltaic array can be determined. Additionally, this understanding can be applied to other neutron sources and used to determine the resulting neutron spectra from any source in any environment.

2.1.1 Neutron Interactions

For low energy interactions between nucleons, the energy per nucleon is approximately 10 MeV or less. This energy region is of interest as it corresponds to commonly used neutron source energies. To examine the individual types of interactions, the formula for a general nuclear reaction is shown in Equation 1, also written as $X(a, b)Y$, where a is the projectile, X is the target, and Y and b are the products where b is typically lighter than Y [7]. In general, for light projectiles with $A \leq 4$, Y will stop in the target material and b is a nucleon or γ that escapes and can then potentially be detected.

$$a + X \rightarrow Y + b \tag{1}$$

The different types of interactions between particles can be explained by examining the different types of projectiles, targets, and products that fulfill Equation 1. For example, if b is a γ, then this interaction is called radiative capture. If a is a γ, then the reaction is called the nuclear photoeffect. Scattering occurs when X and Y are the same nucleus: elastic scattering when the products are in their ground states, and inelastic scattering when either product is in an excited state. These two interactions slow or moderate the neutrons, making absorption of the neutron by the target material more likely. This equation is accurate when describing most interactions, however, there are slight variations. An example of this is a knockout reaction where a and b are the same particle but there is another nucleon ejected, making three products instead of two. Another example is a transfer reaction where one or two nucleons are transferred from the projectile a to the target X, resulting in only one product, Y. Transfer reactions are a type of direct reaction where most of the target's nucleons do not partake in the reaction. This type of reaction is often used to examine the shell structure of the nuclei involved, since they result in a Y that is in an excited state. Occasionally, a and X merge for a short period of time, sharing the energy, before b is expelled. On the other hand, resonance reactions occur when a quasi-bound state is reached between the reactants before b gets expelled [7].

At any given time, any of these reactions are theoretically possible. However, depending on the target and incoming particles, certain reactions have higher probabilities of occurring than others. The measure of this relative probability is known as the cross-section, often denoted σ. Cross-sections play an important role in neutron transport programs, like MCNP, which use the cross-sections to determine the neutron propagation through a material. Cross-sections vary widely with neutron energy and target material.

The reactions discussed previously are important when it comes to analyzing and

shaping a neutron beam, since any matter between the beam source and the target material will change the beam's neutron energy spectrum. If a beam of mono-energetic neutrons is directed towards a material of arbitrary thickness, the beam collected at the back end of the material may have a much lower intensity. The decrease in intensity is directly proportional to the thickness and composition of the material. This intensity loss relationship is given by Equation 2 where dI is the loss in intensity of the neutron beam, I_o is the initial intensity of the beam, σ_t is the total cross section, n is the number of atoms per unit volume of the material the beam traverses, and dx is the material thickness [7].

$$dI = -I_o \sigma_t n dx \tag{2}$$

The cause of the decrease in intensity of the mono-energetic beam is that the neutrons are either scattered or absorbed in the material. This either causes the loss of neutrons in the beam or reduces the energy of a given neutron, but at the same time creates lower energy neutrons. When looking at a single neutron emitted by the beam, it is likely that the neutron will scatter more than once before either being absorbed or making it out of the material to be collected by a detector, assuming that the material is more than a few mean-free-paths thick. The mean-free-path is the average distance a particle travels in a medium before interacting [8]. For neutrons, the mean-free-path is equal to the inverse of the total macroscopic cross-section. The energy distribution of a single neutron scattering more than once is best described as in Figure 5 [7]. Mono-energetic neutrons scatter off carbon-12, creating a spectrum of neutron energies ranging from $0.72E$ to E, as shown in Figure 5(a). This spectrum is then divided into five separate groups, resulting in Figure 5(b). Figure 5(c) shows the calculated energy distribution after the mono-energetic neutron scatters up to four times. As shown, the energy spectrum of the scattered neutron spreads out and

decreases with subsequent scatterings.
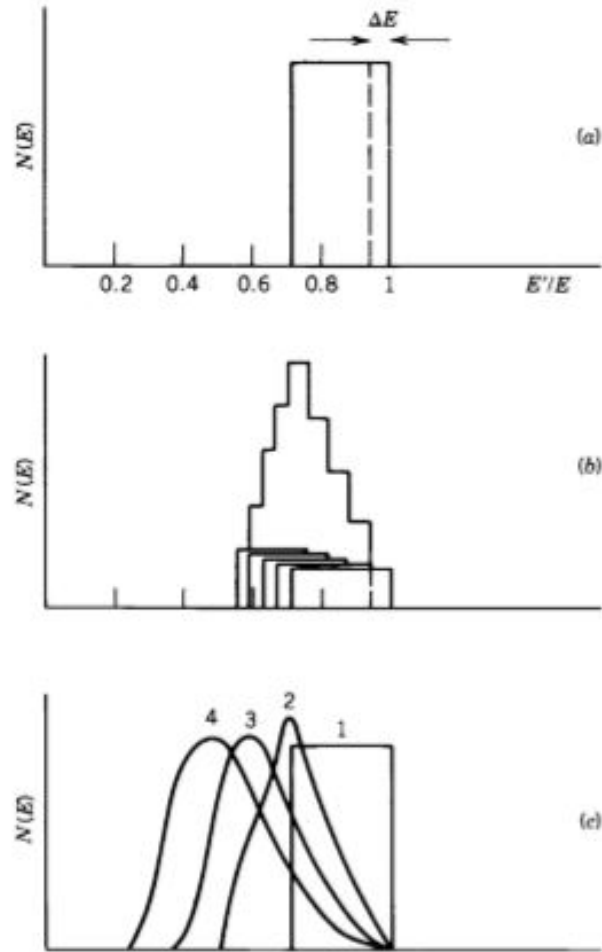
Figure 5. (a) A monoenergetic neutron of energy E gives, after a single scattering from ^{12}C, a flat distribution of laboratory energies E' from $0.72E$ to E. (b) After a second scattering, we get the five flat distributions shown, whose sum is the peaked distribution. (c) An exact calculation of the energy distribution after 1, 2, 3, and 4 scatterings. Reproduced with permission from [7].

When the neutrons approach thermal energies, their speeds become comparable to the thermal motion of the atoms of the material [7]. Thus, it can be assumed that the neutrons reach thermal equilibrium with the atoms in the material after a given amount of time and at a certain temperature if the volume of material is sufficient. Applying statistical mechanics to describe the neutron energy distribution results in a Maxwell distribution function. This function is shown as Equation 3, where $f(E)dE$

11

is the fraction of neutrons with energies between E and $E + dE$, n is the number of neutrons per unit volume, k is the Boltzmann constant, T is the temperature at which thermal equilibrium is achieved, and E is the energy of the scattered neutron. This equation is plotted in Figure 6. When comparing Figure 5(c) and Figure 6, one can observe that the former becomes the latter with significantly more than four neutron scatterings.

$$f(E)dE = \frac{2\pi n}{(\pi kT)^{3/2}} E^{1/2} e^{-E/kT} dE \tag{3}$$
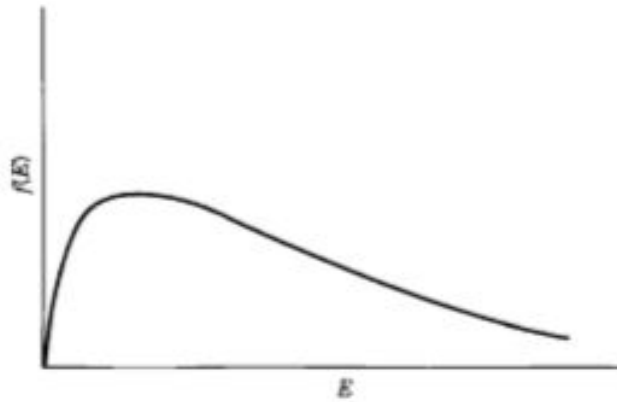
Figure 6. Maxwellian energy distribution representing a neutron energy spectrum after many scatterings. Reproduced with permission from [7].

By studying the interactions mentioned above using neutron beams, nuclear reactors, and smaller planchette sources, the effects of neutron sources that cannot currently be produced, like the neutrons from a nuclear detonation, can be extrapolated through statistical modeling. For example, neutron transport programs have the ability to allow the user to create a scene out of various geometries and materials, and then model the amount and energies of neutrons reaching a certain point or surface some user-defined distance from the source. This location is often denoted as a detector. The source starts the transport process by creating particles of user-

designated energies that propagate throughout the materials and geometries from the source location. This can be done simplistically for small geometries or for large-scale scenarios. Regardless, the particle interactions involved are the same, only the number of interactions is different. For a model that mimics a nuclear detonation, with a potentially large volume of neutron interaction, there will be significantly more interactions involved as compared to modeling the inside of a 4 mm detector crystal. By comparing the source energy spectrum and the energy spectrum of the particles collected at the detector, the differences are explained by the interactions discussed above.

2.1.2 Neutron Activation

A transfer reaction, also known as neutron capture, occurs when the projectile a is a neutron and the product Y becomes a new element, typically in a radioactive state. This process is also referred to as neutron activation. For low-energy incident neutrons, the excited product usually results in a γ emission. Figure 7 shows some of the resulting processes after neutron capture occurs. The excitation energy of the radioactive product A' is equal to the neutron separation energy plus the energy of the incident neutron. In addition, these reactions can be used to determine the energy and spin-parity of the capturing nuclei. The spin and parities are determined via Equations 4 and 5, where I' is the spin capturing state, I is the spin of the original nucleus (X), l is the orbital angular momentum of the neutron, s is the spin angular momentum of the neutron, and π is the parity of the original nucleus [7].
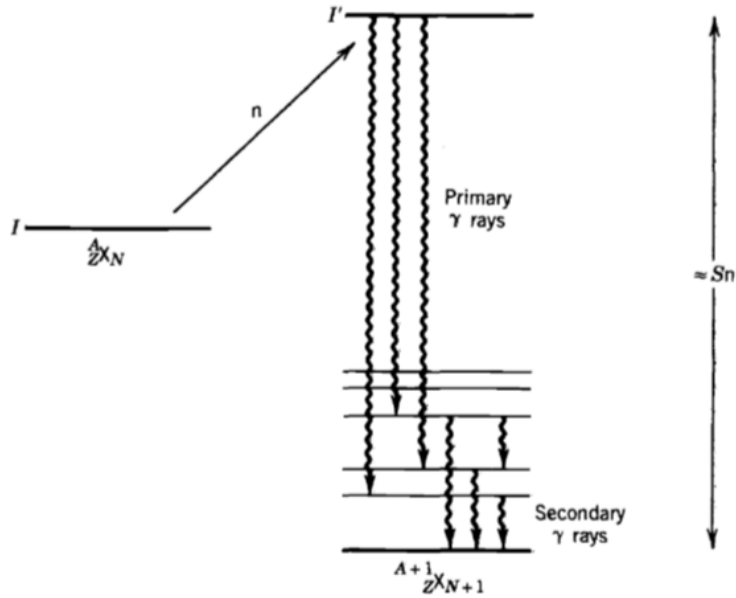
Figure 7. Low-energy neutron capture leads to state I', which then emits a primary γ followed by a secondary γ. Reproduced with permission from [7].

$$I' = I + l + s \tag{4}$$

$$\pi' = \pi(-1)^l \tag{5}$$

Thermal neutrons result in s-wave capture, where the neutron orbital angular momentum l is 0, and $I' = I \pm \frac{1}{2}$ and $\pi' = \pi$ [9]. For the capture state to decay via γ emission, the γ spectrum shows the primary radiations from the capture state to lower excited states and secondary radiations from the lowest excited states to the ground state. These primary and secondary radiations are shown in Figure 7 as the primary and secondary γ rays [7]. It is also common for the neutron capture to result in a radioactive ground state.

These reactions are useful for a multitude of reasons, one of which is neutron activation analysis (NAA). NAA is used to detect the elemental makeup of materials by

examining the characteristic radiation emitted by elements in the material after they absorb neutrons [10] [11]. The analysis is done by exposing a sample of the material to a beam of thermal neutrons, initializing the (n,γ) reaction. The radioactive nuclei produced then emits γ's (prompt γ) or β decays and then emits a γ's (delayed γ) to become stable again. The activity of the sample after irradiation can be calculated according to Equation 6 in $decays/s$, where ϕ is the neutron flux in $neutrons/cm^2/s$, σ is the thermal neutron capture cross section in $barns$, m is the mass of the isotope in $grams$, and A is the isotope mass number of the sample [7]. By applying this equation and an assumption about the efficiency of the gamma spectroscopy detector, the total time required to count to get a resolved gamma peak can also be calculated. Additionally, if the cross-section is known, and the activity can be measured, this equation can be used to calculate an unknown neutron flux. On the other hand, if the flux is known, it can also be used to calculate for unknown cross-sections.

$$Activity = 0.602\frac{m}{A}\sigma\phi(1 - exp(-\lambda t)) \tag{6}$$

By counting the γ rays using a high-purity germanium (HPGe) detector or a similar device, the energies of the prompt and delayed γ rays can be recorded. From this information, the isotopes in the sample can be determined. Additionally, the intensities of the γ ray energy peaks are directly proportional to the amount of the original isotope in the sample [7]. This methodology was utilized to characterize the neutron spectrum near the core of the FBF at OSU-NRL, the results of which were discussed in Chapter 1.

2.1.3 Neutron Particle Transport

To better understand how transport programs like MCNP work, it is critical to understand the theory behind neutron transport as a whole. Transport theory in gen-

eral is based on the Boltzmann transport equation and its solution which describes the transport of neutral particles as they collide with one another [12]. For clarity, the Boltzmann transport equation is shown as Equation 7. When looking at the terms, the Boltzmann transport equation accounts for the rate of accumulation of neutrons by subtracting the rate of leakage out of the volume, subtracting the total interaction rate due to absorption or scatterings, adding the total fission rate which produces a given energy spectrum, and finally adding the differential scatterings of the neutrons. With seven independent variables, solving the Boltzmann transport equation analytically is not achievable. The difficulty of solving this equation can be reduced by making assumptions, but this makes the application less practical. It can also be approximated for very limited applications in terms of the diffusion theory approximation. However, this approximation is typically only used for describing neutron transport in reactors since it assumes the neutrons are monoenergetic. Because of these limitations, numerical techniques are required to get realistic solutions of the Boltzmann transport equation.

$$
\begin{aligned}
\frac{1}{v(E)}\frac{d\Phi(\overrightarrow{r}, E, \overrightarrow{\Omega}, t)}{dt} =& \\
& -\overrightarrow{\Omega} \cdot \overrightarrow{\nabla}\Phi(\overrightarrow{r}, E, \overrightarrow{\Omega}, t) - \Sigma_t(\overrightarrow{r}, E, \overrightarrow{\Omega})\Phi(\overrightarrow{r}, E, \overrightarrow{\Omega}, t) \\
& + \chi(E)\int dE' \int d\Omega' v\Sigma_f(\overrightarrow{r}, E', \overrightarrow{\Sigma'})\Phi(\overrightarrow{r}, E', \overrightarrow{\Omega'}, t) \\
& + \int dE' \int d\Omega' \Sigma_s(\overrightarrow{r}; E'; \overrightarrow{\Omega'} \rightarrow \overrightarrow{\Omega})\Phi(\overrightarrow{r}, E', \overrightarrow{\Omega'}, t) \quad (7)
\end{aligned}
$$

The most commonly used numerical technique is the Monte Carlo method. Mathematicians John von Neumann and Stanislaus Ulam proposed a solution that combined the probabilities of each possible interaction the particle could undergo in a material with random sampling techniques to create a 'random walk' for each par-

ticle [12]. Using a roulette wheel to do the hard work, Monte Carlo techniques do not solve the Boltzmann transport equation, but instead simulate the behavior of the particles through space. The random sampling techniques involve probability density functions for each possible particle interaction. This interaction parameter, x, has a distribution as shown in Equation 8. A number is then randomly selected between 0 and 1 that is assigned to x, which determines whether a specific interaction event occurs for the particle in question.

$$p(x) = 1 \qquad 0 \leq x \leq 1 \tag{8}$$

Statistically, the Monte Carlo solution is an approximation for the unique solution that has a corresponding confidence interval in which the correct answer lies [12]. Additionally, the statistical uncertainty associated with this numerical method is indirectly proportional to the simulated number of particles. The accuracy of the approximation improves according to the law of large numbers. When more samples are taken, the average of those samples gets closer to the "true" mean. This average is shown in Equation 9, where N is the number of samples, x_i is the recorded variable for the ith sample, and $\overline{x}$ is the mean or average of the variables.

$$\overline{x} = \frac{1}{N} \sum_{i=1}^{N} x_i \tag{9}$$

Physically, the Monte Carlo process can be described in a few steps. First, the particles are introduced into an environment by a source. The particles are tracked through the environment where both the energy and direction of each particle is randomly sampled from their corresponding probability distribution functions [12] [13]. Additionally, the type of interactions for each particle are randomly sampled using the associated cross-sections for each interaction. It should be noted that the

types of interactions treat the particle differently: scatterings change both the energies and directions of the particles, and leakages, captures, and fissions end the current particle's transport and start the transport of the next particle. The final result is a total count of particles that make it through the environment to a desired location.

MCNP, one of the most commonly utilized Monte Carlo based programs, is a "general-purpose, continuous-energy, generalized-geometry, time-dependent, Monte Carlo radiation-transport code designed to track many particle types over broad ranges of energies," developed by Los Alamos National Laboratory (LANL) [14]. MCNP6 is the most recent version of MCNP and is the merge of MCNP5 and MC-NPX. This version includes new features and capabilities including, but not limited to, an expansion of particle types to include heavy ions, updated high-energy physics models, muon capture physics, LLNL photofission and neutron fission multiplicities, double differential particle interaction cross-section generator, and more.

A single MCNP6 input deck consists of three sections: cell cards, surface cards, and data cards. The cell card is where the cells for each of the surfaces is created. The surface card creates the surfaces that make up the cells from the previous section. This includes the shape and its corresponding dimensions for each surface. Lastly, the data cards consist of the material makeup of each surface, the source information, the tallies, and the number of particles. The tallies are chosen based on the type of data the user is looking for. For example, the F2 tally calculates the flux averaged over a surface that the user also chooses.

2.1.4 Neutron Detection

Neutron detection utilizes the interactions discussed previously. There are three categories of commonly used neutron detectors, one of which is gas-filled detectors. Gas-filled detectors consist of a chamber filled with gas that also has an electrode on

each end with an applied potential difference between the two electrodes [15]. When radiation interacts with the gas, it ionizes and creates ion pairs inside the chamber. The cations are attracted to the cathode and the anions to the anode, creating a pulse that can be measured. This process is shown in Figure 8. There are three types of commonly used gas-filled detectors: ionization chambers, proportional counters, and Geiger-Mueller (GM) counters. The processes of these three detectors are similar, however they vary in magnitudes of applied voltage and geometries.
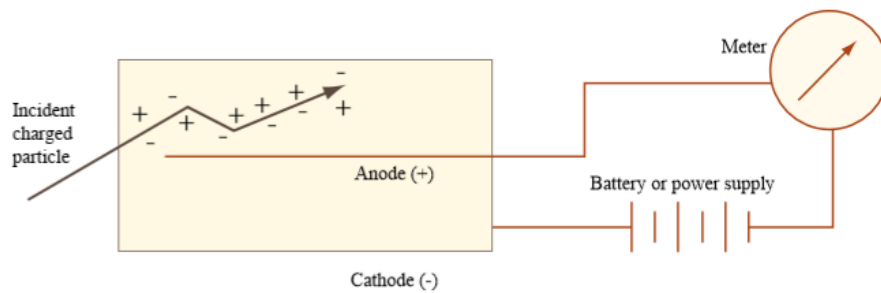
Figure 8. Schematic of a gas-filled detector. Reproduced with permission from [15].

Semiconductor detectors are also commonly used neutron detectors. Similar to gas-filled detectors, semiconductor detectors rely on ionization by the incident radiation. However, instead of a gas-filled chamber, the material is a solid material with a crystal lattice and the ionization creates electron-hole pairs rather than ion pairs [16]. Since standard semiconductor materials do not have high neutron absorption cross-sections, a neutron reactive layer is typically applied on the outside of the semiconductor. This material utilizes neutron reactions to convert the neutron into a reaction product that enters the semiconductor and creates the electron-hole pairs. This process is shown in Figure 9 [17]. These electron-hole pairs are then collected, creating an electrical signal that can be detected.
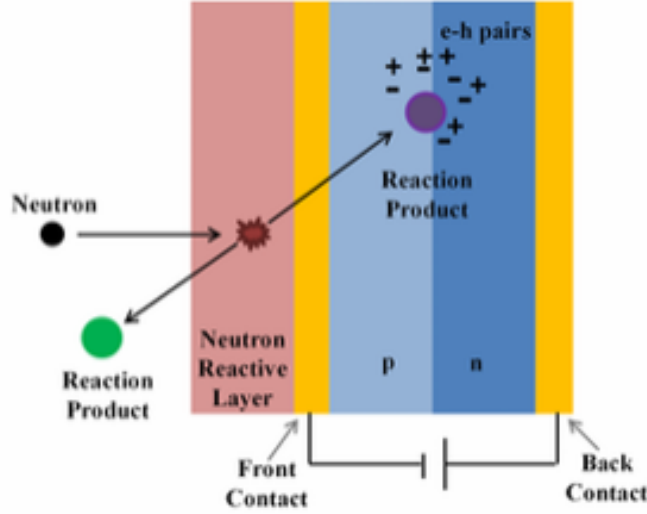
Figure 9. Simple device design of a semiconductor detector. Reproduced with permission from [17].

Lastly, scintillation detectors are also commonly used for neutron detection. Scintillation detectors work quite differently than the other two types of detectors. The incident neutron interacts with the scintillator, creating a charged particle, an alpha particle, or a high-energy photon that excites electrons in the scintillator, changing the electron configuration [18]. The various excited states for an organic molecule, including the singlet states, $S_{\#}$, triplet states, $T_{\#}$, and the vibrational states, $S_{\#\#}$, are shown in Figure 10 [8]. Typically, a molecule excited to a state higher than the S_1 singlet state de-excites on the order of picoseconds via internal conversion to the S_{10} state. The prompt fluorescence, or optical photon, emitted by the scintillator is caused by the de-excitation of the S_{10} state to one of the various ground states [8]. The photon interacts with the photocathode which then releases an electron. This electron is accelerated toward a dynode by a voltage potential. When it interacts with the dynode, additional electrons are released. These electrons are accelerated toward a second dynode that results in the release of more electrons. This process amplifies the current by multiplying the amount of electrons produced from a single

20

photon interaction. The current is then strong enough to create a pulse that can be detected. This process is shown in Figure 11. Occasionally, intersystem crossing occurs where the excited singlet state is converted to a triplet state. This process is shown on the right side of Figure 10. This state can also de-excite to produce a delayed optical photon, often called phosphorescence. These photons typically have lower energy than those created in the fluorescence.
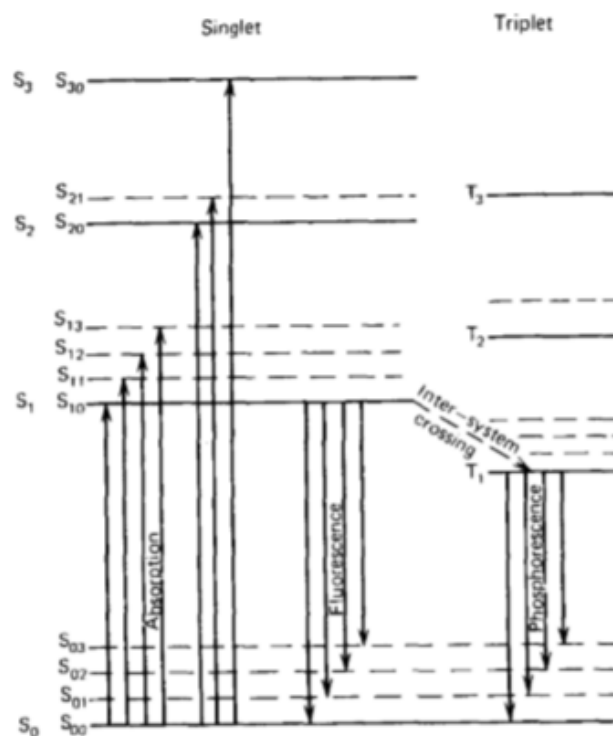
Figure 10. Electron energy levels of an organic molecule. Reproduced with permission from [8].
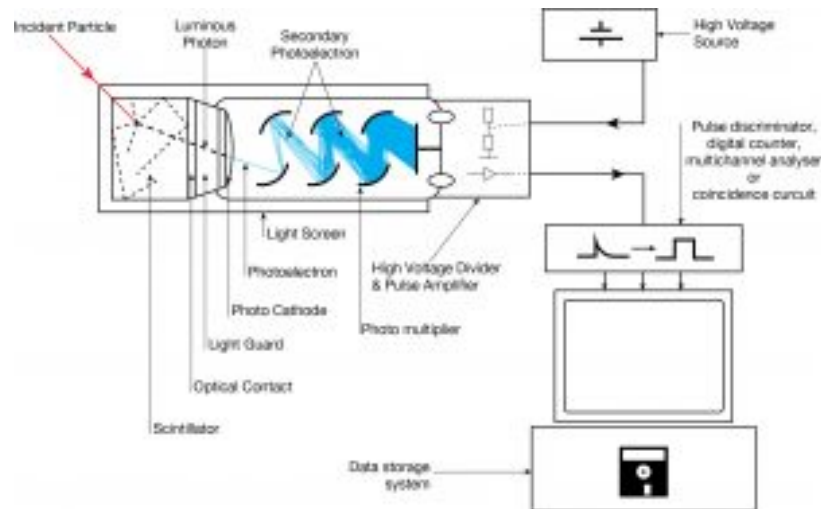
Figure 11. Schematic of a scintillation detector. Reproduced with permission from [18].

Inorganic scintillators operate similarly to organic scintillators, following electron excitation and de-excitation. One of the principles that sets inorganic scintillators apart are added impurities. These impurities, also called activators, in the crystal lattice allow the wavelength of the emitted optical photon to be controlled by changing the energy band structure of the scintillator by reducing the energy of the transition from the conduction band to the valence band. This process is shown in Figure 12 [8]. The historical example of this phenomenon is sodium iodide. By adding thallium iodide to the crystalline sodium iodide, the light produced in the scintillator was significantly larger than that produced by organic scintillators of the time [8].
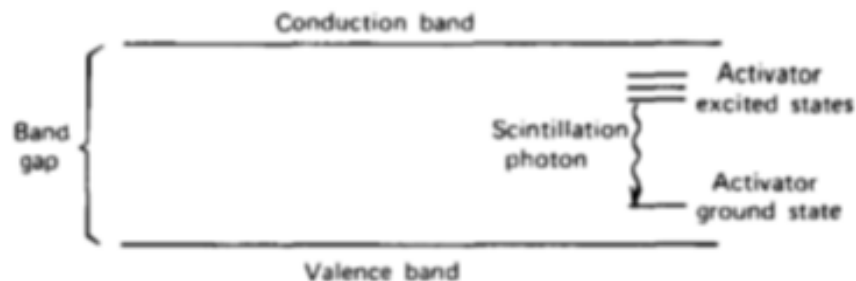
Figure 12. Activated scintillator energy band structure. Reproduced with permission from [8].

Most detectors have two different modes that they can operate in: pulse and current mode. Pulse mode processes the signal generated from each interaction separately, whereas current mode averages the signals together to create a net current signal [15]. Pulse mode, the more commonly used of the two modes, requires a time separation between two pulses so that the signal is distinct. This time separation is referred to as the dead time of the detector and it is highly dependent on the system. For a paralyzable system, a pulse that occurs during the dead time extends the dead time. This is problematic for any source with a high neutron flux as the interaction rate will be too high for the detector to count more than one interaction. For a non-paralyzable system, the dead time is not extended when a pulse occurs during the dead time caused by the previous pulse, making this system the most ideal for sources with high neutron fluxes. The concepts of a paralyzable and non-paralyzable systems is shown in Figure 13 [15]. Furthermore, Figure 14 shows the relationship between the count rate of a detector and the interaction rate for ideal non-paralyzable, and paralyzable detectors.
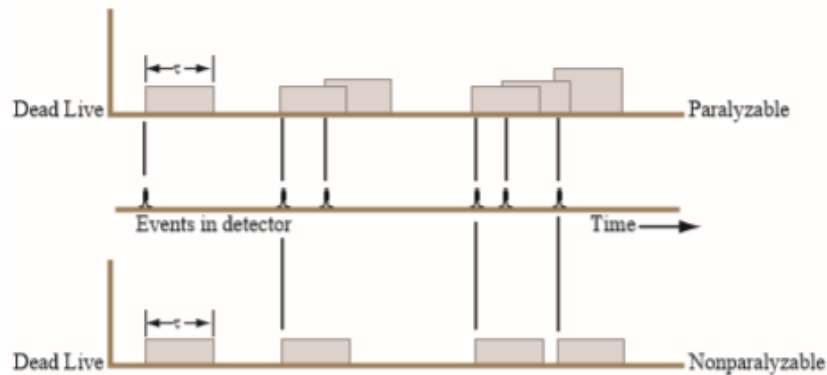
Figure 13. Depiction of how paralyzable and nonparalyzable systems operate. Reproduced with permission from [15].
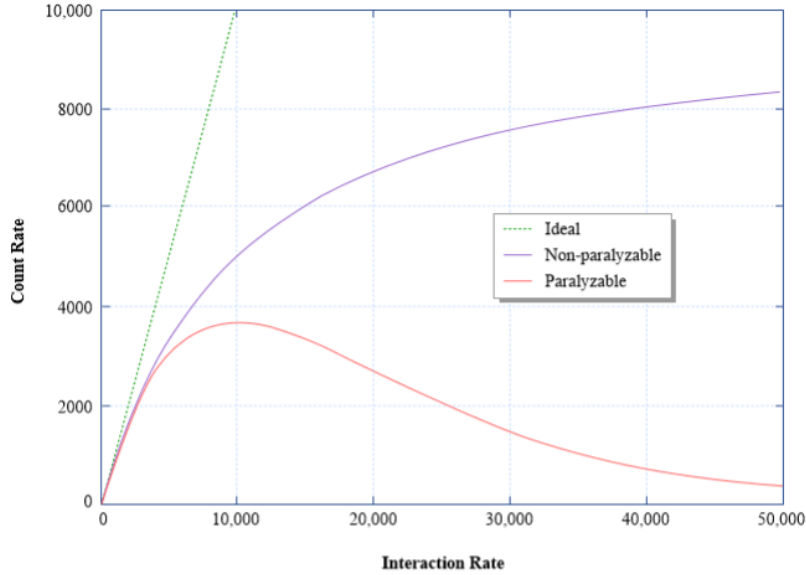
Figure 14. Relationship between the count rate and interaction rates for various types of detecting systems. Reproduced with permission from [15].

Another important aspect of neutron detection is the efficiency of the detector. The efficiency, also referred to as the sensitivity of the detector, is a determination of the detectors ability to detect radiation [15]. For detectors in pulse mode, the efficiency is equal to the probability that the incoming particle will interact with the detector medium and a pulse will be created and collected. Detector efficiency is typically broken up into two parts: geometric efficiency and intrinsic efficiency. Geometric efficiency, like the name entails, depends on the geometry of the detector and source positioning and is approximately equal to the number of particles reaching the detector over the number of particles emitted by the source. This relationship, defined by the solid-angle Ω between the source and detector, is shown in Figure 15. Intrinsic efficiency is dependent on the material makeup of the detector and is proportional to the ratio of number of particles emitted to the number of particles reaching the detector.
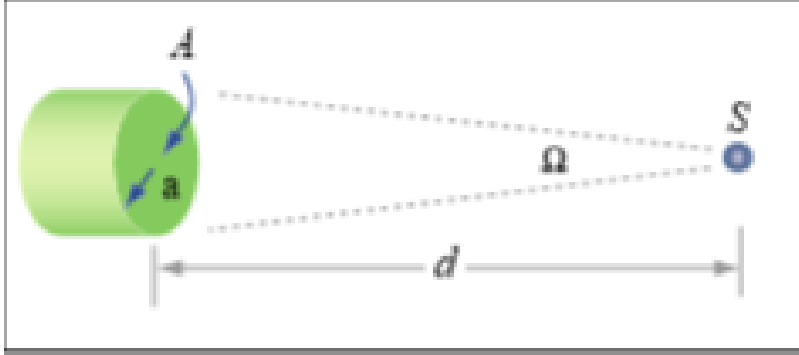
Figure 15. Geometric efficiency depends on the solid-angle Ω, where the detector A is some distance d from the source S. Reproduced with permission from [15].

Since neutrons do not directly ionize materials, they depend on reactions like (n,p), (n,γ), or (n,α) for the ionization to occur. For this reason, neutron detectors will either have a conversion region or the detector will consist of a material with a high cross-section for a neutron reaction. For fast neutron detection, the (n,p) reaction is generally relied on for signal generation. However, for thermal neutrons, the primary reactions for signal generation are the (n,γ) and (n,α) reactions. For this reason, materials with high thermal neutron absorption cross-sections are used. Lithium-6 (^{6}Li) has a high absorption cross-section for thermal neutrons at 941 barns for the reaction shown in Equation 10. The energy dependent cross section is shown in Figure 16.

$$n + {}^6 Li \rightarrow {}^4 He + {}^3 H + 4.78 MeV \tag{10}$$
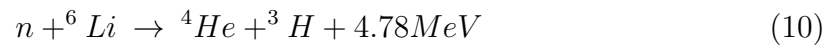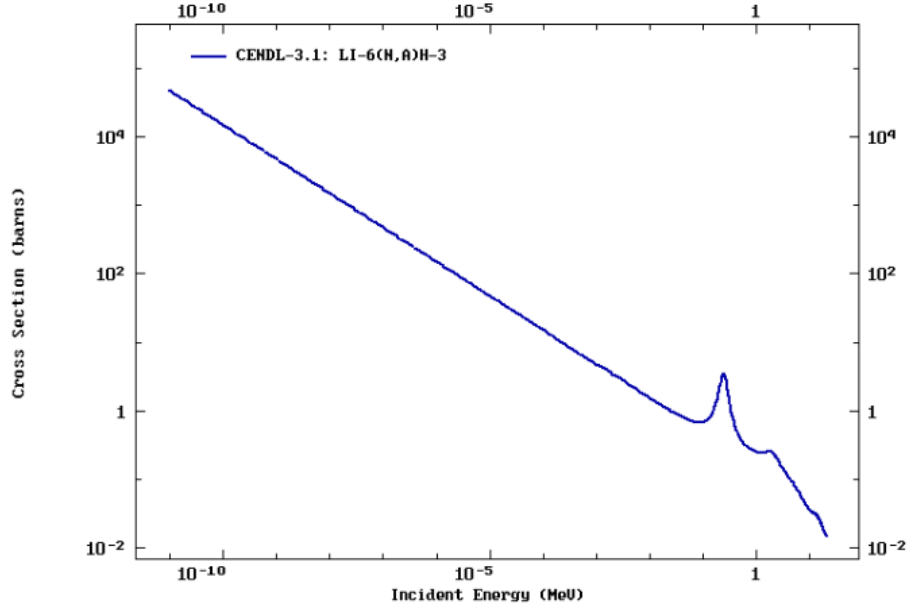
Figure 16. $^6Li(n, \alpha)$ **reaction cross-sections** [19]**.**

Although ^{6}Li is a useful material for detecting thermal neutrons, it is not as efficient at detecting fast neutrons due to the lower reaction cross-section for this region. However, fast neutrons can be moderated down to thermal regions and then interact with ^{6}Li, where the probability for the (n,alpha) reaction is high. One of the more commonly used moderating materials is polyethylene. This is due to its high hydrogen content and low impurities. Hydrogen is very efficient at moderating neutrons because its mass is near equal to the mass of a neutron. When a neutron interacts with hydrogen, a large portion of its energy can be transferred to the hydrogen nucleus, substantially reducing the energy of the incident neutron. As shown in Figure 17, it takes approximately ten collisions with hydrogen nuclei to reduce the energy of the incident neutron by a factor of one thousand.

With moderating materials, ^{6}Li can also be used to detect fast neutrons. The neutron detection efficiency of a ^{6}LiI(Eu) crystal is dependent on the moderation of the neutron energy and is shown in Figure 18. As shown, the efficiency of the scintillator increases with increasing moderator thickness [20]. This shows that the

integrity of the detector holds when used with various sized polyethylene spheres. Further deconvolution analysis is needed to determine the neutron spectrum when detecting moderated neutrons. This process is discussed later in this chapter.
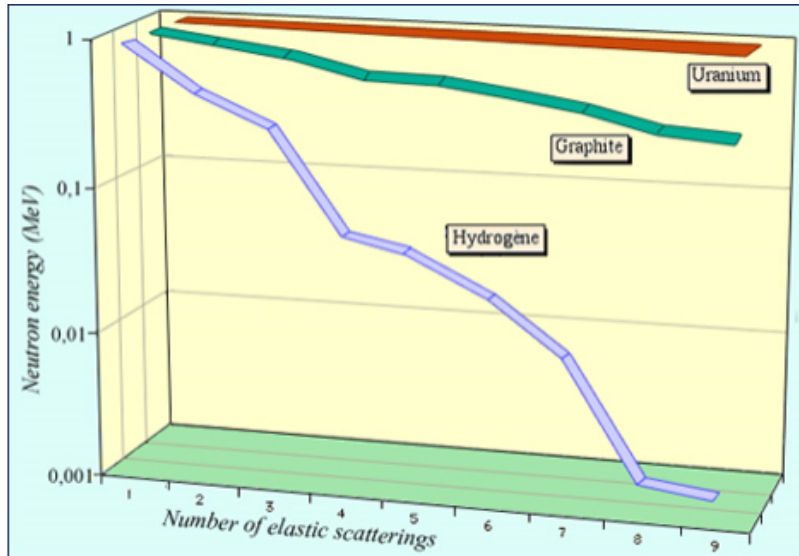
Figure 17. The effects of neutron scatterings on neutron energy for various materials. Reproduced with permission from [21].
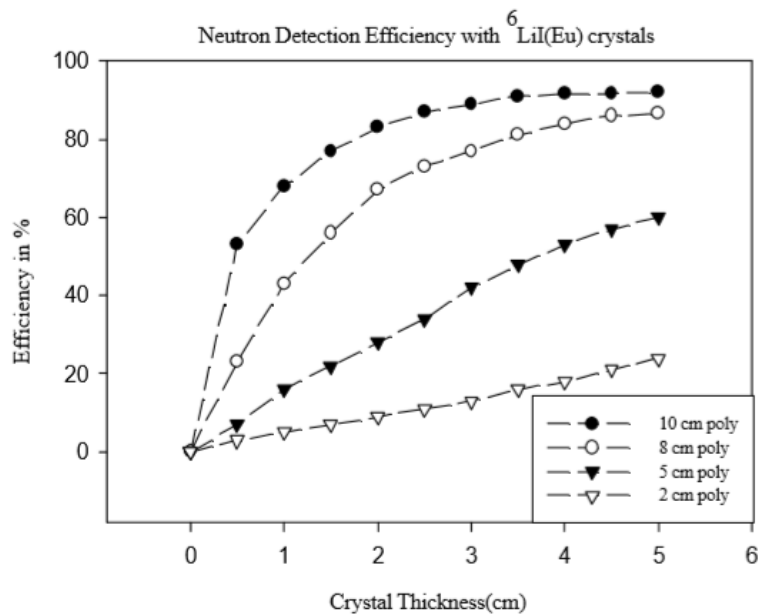
Figure 18. Thermal neutron detection efficiency by different thicknesses of ^{6}LiI(Eu) crystal. Layers of various thicknesses of polyethylene rings were used to optimize the neutron energy moderation. Reproduced with permission from [20].

This research involves a LiI(Eu) scintillation detector where the ionizing radiation interacts in the detector to produce UV and/or visible light [15]. A scintillating detector was chosen over the other common detectors because they are known for their high conversion efficiency which produces high energy resolution. Additionally, they are relatively inexpensive compared to other detectors. The LiI(Eu) crystal used was enriched to 96% ^{6}Li (natural lithium is only 6% ^{6}Li) to detect thermal neutrons. The europium in the crystal acts as an activator. The purpose of the activator is to lengthen the wavelength of the light emitted by the scintillator. The activator does this by reducing the energy required to jump the band gap and therefore reduces the energy of the resulting photon that is emitted [22].

2.2 Neutron Spectrum Unfolding

2.2.1 Bonner Sphere Spectrometer

Introduced in 1960, the Bonner sphere spectrometer, or BSS, measures neutron spectra using a 4mm by 4mm LiI(Eu) scintillator crystal [23]. Capitalizing on the thermal neutron cross-section of ^{6}Li in the LiI(Eu) crystal, the detector operates interchangeably within the center of polyethylene spheres of varying sizes. The spheres, with diameters ranging from two to twelve inches, allow neutrons with energies ranging from 0.025 eV to approximately 10 MeV to be measured by the LiI(Eu) crystal. For this reason, BSS are typically involved in characterizing unmoderated reactors [6].

There are a few factors that affect the BSS and its response, efficiency, and energy resolution. Although the larger spheres are necessary to moderate fast neutrons to thermal energy ranges, they also increase the chance of a lower energy fast neutron being absorbed before reaching and interacting with the detector crystal. This is shown in Figure 19. Additionally, when an incident neutron collides with a hydrogen

nucleus in the polyethylene sphere, it can potentially be deflected back out of the sphere and never reach the detector crystal. This is also shown in Figure 19. Systematically, the BSS also suffers from low-energy resolution due to the loss of information about the incident neutron energy. This is caused by the variation in the number of collisions occurring in the moderating spheres. Due to this, the average energies of the neutrons are calculated for each sphere. The capture reactions in the detector crystal are also indistinguishable, furthering the loss of information about the energy of the incident neutron [6].
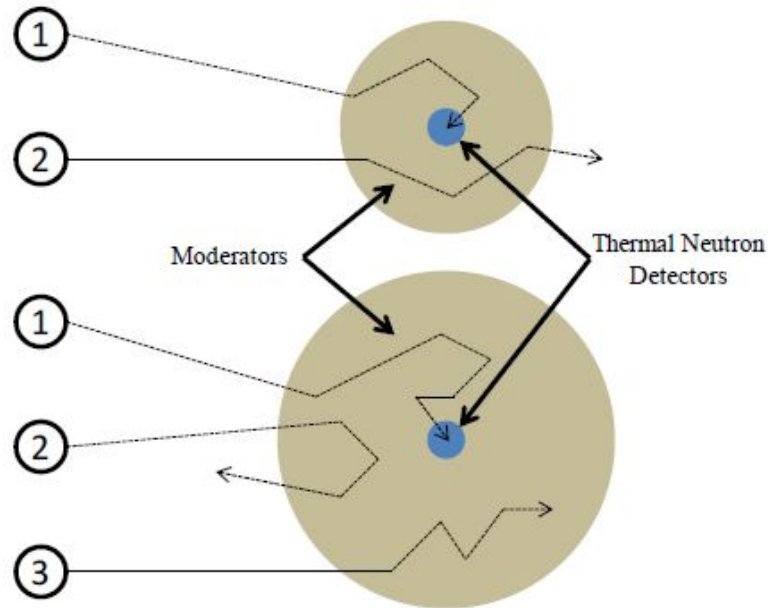
Figure 19. Depiction of the possible neutron paths when interacting with the Bonner Sphere spectrometer with two varying sized polyethylene sphere moderators [23].

To ensure the accuracy of the BSS in detecting neutrons, the system should be calibrated accordingly. The Environmental Measurements Laboratory (EML) recommends that the calibration be done with the National Institute of Standards and Technology (NIST) monoenergetic neutron beams. However, AFIT does not have this capability so the calibration must be done with different sources. The EML also recommends that the normalization of the response matrix of the detector be performed

using a ^{252}Cf fission neutron source in an open air calibration facility. This limits the ground and air scattering to approximately 3% of the total contribution of neutron moderation [6]. This step is not necessary as the response functions were determined using MCNP modeling. The BSS can also be calibrated in a regular laboratory with a standard neutron source, like ^{241}Am, to determine the optimal operating voltage [5].

The BSS is chosen to conduct the neutron detection in this research due to its versatility and mobility. AmBe neutron sources emit neutrons with an average energy of 4.2 MeV and a maximum energy of 11 MeV via the reaction shown in Equation 11 [24], where the reactant α is emitted by the radioactive ^{241}Am. This high energy range of neutrons makes the AmBe source viable in testing the BSS's efficiency at detecting higher energy neutrons. After effectively detecting the neutrons emitted by the AmBe source at AFIT, the BSS will be used to characterize the broader energy range of neutrons emitted by the FBF at the OSU-NRL in future research.

$$^{9}Be + \, ^{4}He \rightarrow \, ^{12}C + \, ^{1}n + \gamma \tag{11}$$
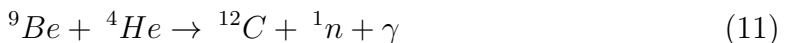
2.2.2 Spectrum Unfolding Programs

To determine the neutron spectrum of a source, the raw data collected by the scintillator must be deconvoluted or unfolded. The unfolding is done by relating the number of interactions recorded in the detector (counts) to the neutron flux energy spectrum. This relationship is defined as the response function of the detector and a discussion of neutron flux is required to examine it fully. Neutron flux is defined as the rate of flow of neutrons. Specifically, it is the density of neutrons that has traveled a set distance in space in a given amount of time, resulting in units of $neutrons/cm^{2}/sec$ [25]. Equation 12 shows the neutron reaction rate density, ρ_n, in

terms of the macroscopic cross section for the given interaction for neutron energy E, $\Sigma(E)$, and the neutron flux at time t for neutron energy E, $\phi(E, r, t)$ [23].

$$\rho_n = \Sigma(E)\phi(E, r, t) \tag{12}$$

When the neutron energy flux and the counts are known, the detector response can be determined via Equation 13, where B_i is the number of counts for the ith detector setup, ϕ_g is the differential neutron flux for the gth energy group, $R_{i,g}$ is the response of the ith detector to the gth energy group, and ΔE_g is the width of the energy bin of the gth group [23]. Solving this equation for $R_{i,g}$ gives the response function for one detector setup. For the BSS, the response matrix is the response function of each polyethylene sphere setup including the setup without a sphere (bare detector) compiled into a single matrix. The matrix is determined using MCNP by modeling each BSS setup and creating a neutron source with a known energy flux. The input code of the model is attached in the appendix. An example of the response functions is shown in Figure 20 [26].

$$B_i = \sum_{g=1}^{n} \phi_g R_{i,g} \Delta E_g \tag{13}$$

31
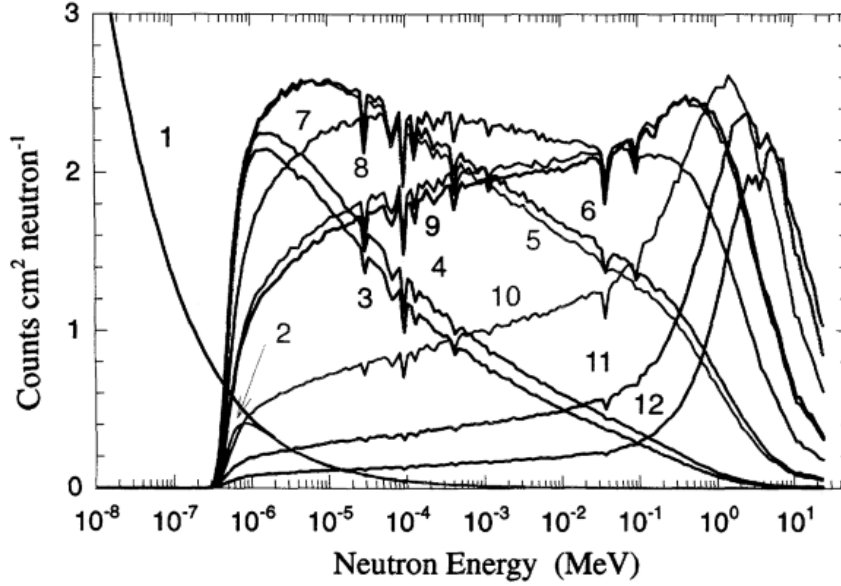
Figure 20. Calculated response functions of EML multisphere neutron spectrometer detectors of varying sizes with BF_3 counters. Reproduced with permission from [26].

$$N_k + \epsilon_k = \sum R_{ki} f_i \qquad (14)$$

The program Maximum Entropy Deconvolution (MAXED) is specifically designed for the BSS and uses the relationship in Equation 14 to determine the neutron energy spectrum of a source, where N_k is the counts, R_{ki} is the discretized response function, ϵ_k is the unknown measurement error, and f_i is the discretized neutron spectrum. This relationship is applied to each detector setup, k [26]. Finding a unique solution $f(E)$ requires more information for MAXED. An initial estimate, or *a priori* spectrum, must be input to MAXED so that it can be modified by the new data. MAXED then uses the modified spectrum as the best estimate of the neutron spectrum from the source. The best estimate will be close to the true neutron spectrum if an accurate *a priori* spectrum is used. The solution with the largest degree of entropy, S, is the best solution. This value is calculated as shown in Equation 15, where f_i^{DEF} is the *a priori* discretized spectra [26]. This is MAXED's way of keeping the unfolding

32

process unbiased and consistent and it is the mathematical basis for the spectrum deconvolution [23].

$$S = -\sum [f_i \ln (f_i/f_i^{DEF}) + f_i^{DEF} - f_i] \tag{15}$$

Finally, MAXED carries out the error of the spectrum unfolding by combining the unknown uncertainties, ϵ_k, and the standard deviations of the measurements, σ_k, into a chi-squared statistic, shown as the left-side of Equation 16, where Ω is usually equal to the number of detectors [26]. It should be noted that this equation assumes that the unknown errors, ϵ_k, are normally distributed with a mean equal to zero and that the variances of the unknown errors are equal to σ_k^2. The chi-squared value thus provides an indicator of the goodness-of-fit of the spectrum to the actual recorded data. Further information on the MAXED unfolding algorithm can be found in the MAXED technical report [26]. An example of a neutron spectrum unfolded using MAXED is shown in Figure 21, where the units for the y-axis is fluence per lethargy ($neutrons/cm^2$). The fluence per lethargy is defined as the time integrated neutron flux divided by the logarithmic ratio of the initial neutron energy to the moderated neutron energy. According to the technical report, this example unfolding resulted in a chi-square value of 8 for the maximum entropy spectrum and 262 for the default spectrum. These values seem quite high compared to normal chi-squared statistics where any value below one is desired. This is because MAXED relies on the *a priori* spectrum to unfold. The chi-squared statistic is therefore entirely dependent on the accuracy of the *a priori* spectrum. If the *a priori* spectrum is close to the true spectrum of the source, the chi-squared value will be close to 1. However, if there is not enough information about a neutron source or it has not been characterized by other means, the *a priori* spectrum may be very different than the true source spectrum. This will result in a high chi-squared value that is directly proportional

to the difference between the two spectra. In conclusion, MAXED is a viable tool in unfolding neutron spectra for the neutrons collected with a BSS.

$$\sum \epsilon_k^2/\sigma_k^2 = \Omega \tag{16}$$
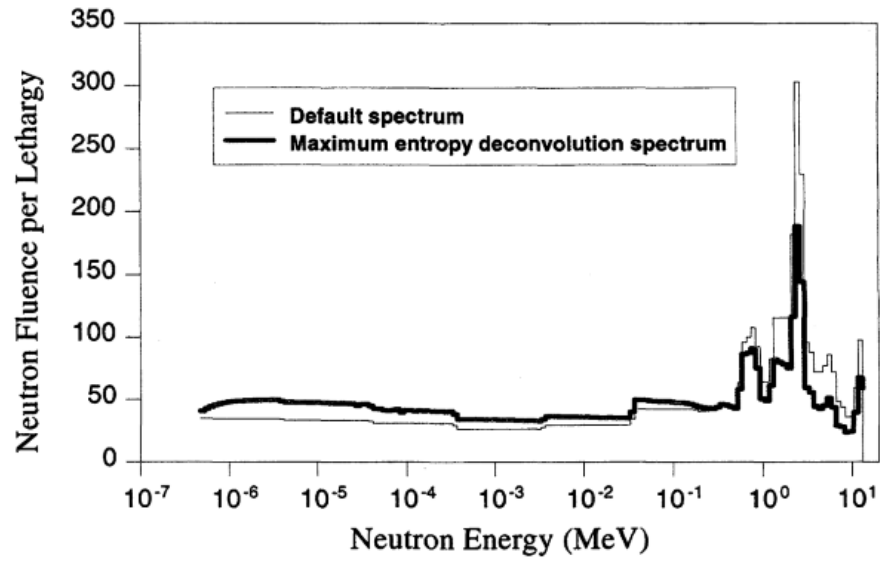
Figure 21. Default and MAXED spectrum for an example discussed in the MAXED technical report. Reproduced with permission from [26].

III. Methodology

3.1 BSS Response Functions

MAXED requires the response functions for the detector used in counting the neutrons. Since it is difficult to find sources that have a wide range of neutron energies with relatively similar fluences, the response functions are determined via simulation with MCNP6. Using the same model from Decker in 2014, the model created in MCNP6 is shown in Figure 22 [23]. As shown, the source is a parallel beam of mono-energetic neutrons. Using the F4 tally, MCNP outputs the neutron flux averaged over the detector surface. This model is run with various neutron energies for each configuration of the polyethylene spheres to produce the response function for each setup. The MCNP6 output is then plotted, as shown in Figure 23.
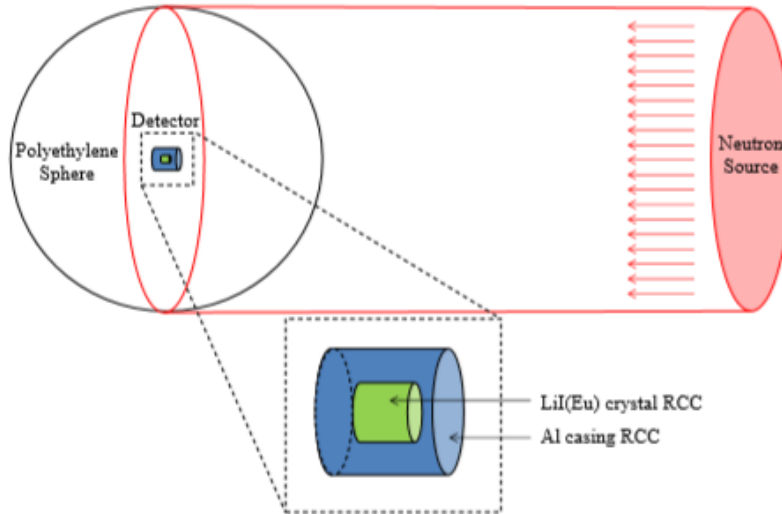
Figure 22. Diagram of the computational model used by MCNP6 to reproduce the response function for each moderated sphere [23].
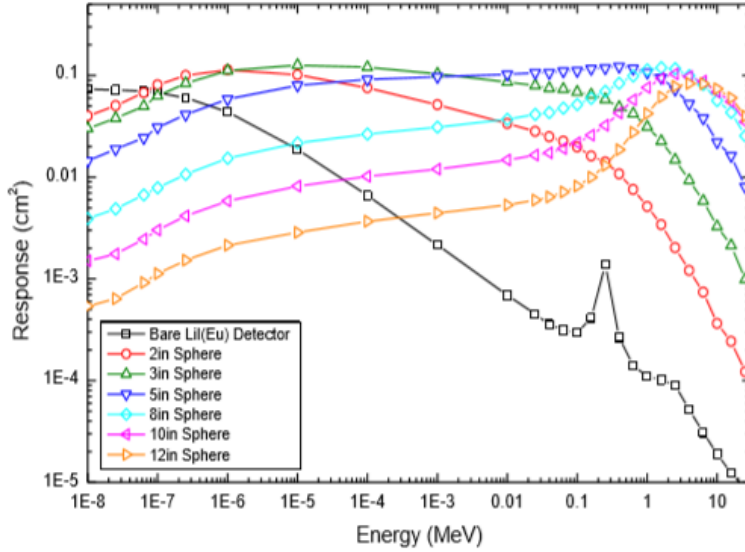
Figure 23. BSS response matrix derived using MCNP6, based upon input parameters described by Mares and Schraube [23].

Figure 23 shows that the bare detector captures significantly more low-energy neutrons than higher energy neutrons. Most of the higher energy neutrons do not get absorbed by the detector when there is no moderator around it. The anomalous peak just below 1 MeV corresponds to the peak in the (n,α) absorption cross-section in ^{6}Li, shown in Figure 16. The response function of the bare detector follows the shape of the ^{6}Li (n,α) absorption cross-section plot nearly identically. The only difference occurs from 10^{-8} to 10^{-6} MeV where, instead of being linear, the response function plateaus. This is likely due to the fact that the detector crystal is not completely made-up of ^{6}Li. Instead, 4% of the crystal consists of iodine and europium. These two elements have noticeably high absorption cross-sections, as shown in Figures 24 and 25 where both ^{127}I and ^{153}Eu are mostly dominated by the (n,γ) reaction in this region [19]. Although the cross-sections for both are still significantly lower than the 941 barns (n,α) cross-section for ^{6}Li, they still factor into the total probability of interactions inside the crystal. As such, the resulting γ's that are produced may not have enough energy to create a light pulse in the detector. Therefore, these

36

interactions are not counted. Another possible cause of this anomaly is the thickness of the crystal. Neutrons with low energies may be interacting with the crystal on the edge of the material. If the light pulse emitted by the resulting interaction is too low, the detector will not count it. These interactions can also be applied to the analysis of the other detector response curves as well since the other configurations also appear to have a drop-off response in this energy range.
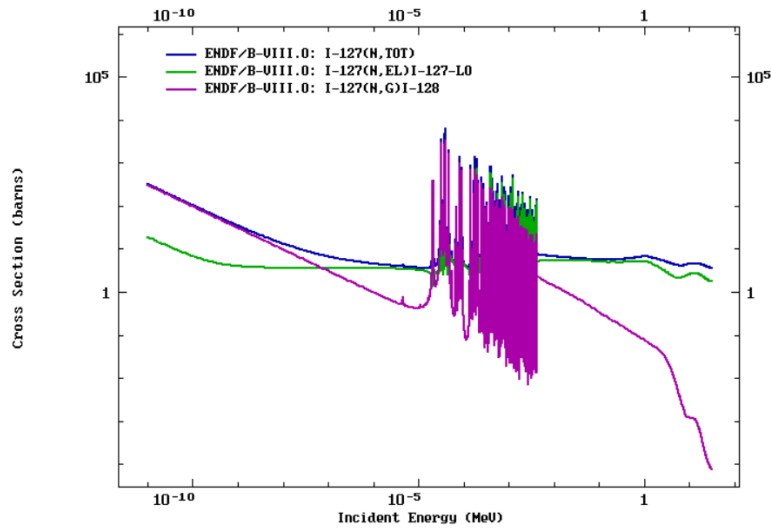
Figure 24. Neutron absorption cross-sections for ^{127}I [19].
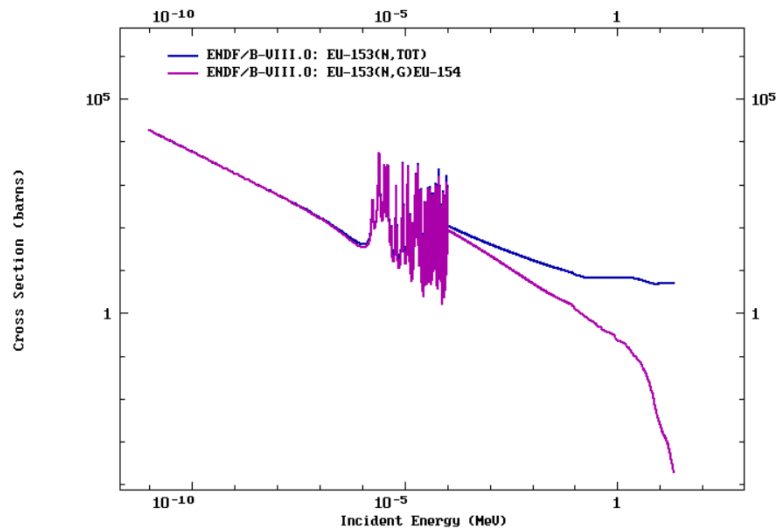
Figure 25. Neutron absorption cross-sections for ^{153}Eu [19].

The two and three-inch sphere setups have similar response functions. The two-inch sphere has a slightly higher response for the low-end of the spectrum, whereas the three-inch sphere has a significantly higher response for neutron energies above 10^{-5} MeV. Because of the lack of characteristic features in these spectra for the low and high energy ranges, these two spheres are useful in characterizing neutrons with energies between 10^{-7} and 10^{-3} MeV.

Starting with the five-inch sphere, the maxmimum response occurs for fast neutron energies around 1 MeV, as shown in Figure 23. At this thickness, neutrons with energies just below 1 MeV are being moderated enough by the sphere to interact in the detector crystal and are counted. There is still a large response for neutrons with energies above 10^{-3} MeV for this sphere, showing that the five-inch sphere setup is still thin enough for lower energy neutrons to make it to the detector crystal without getting absorbed by the sphere.

The eight-inch sphere shows a shift in the maximum response from that of the five-inch sphere. Physically, this shows that as the moderator thickness increases, the detector counts more interactions involving neutrons with energies above 1 MeV. The maximum response occurs between 1 and 2 MeV for the five-inch sphere. The response falls off drastically for neutrons with energies lower than 0.3 MeV, signifying that most of the neutrons below this energy threshold get absorbed by the moderating sphere or deflected away from the detector in the center.

The 10 and 12-inch spheres have similar characteristics to the eight-inch sphere response curve. The major differences lie in the maxmimum response location and the significant reduction to the response for energies below the maximum value. The 10-inch sphere has a maximum response around 3 MeV whereas the 12-inch sphere has a maximum around 5 MeV. It should be noted that the maxima of both the 10-inch and 12-inch spheres are lower in terms of response magnitude than the eight-inch

response peak. This is likely due to the fact that more neutrons are being absorbed by the moderator as it thickness increases. In addition, more neutrons with energies above the peak values are thermalized and react with the detector crystal. This is shown by the slight increase to the response functions above 2 MeV.

In conclusion, the response functions provide valuable information about the neutron interactions within the polyethylene spheres by showing the moderation principle in action. Additionally, the response functions for all of the detector setups make-up the response matrix that is utilized by MAXED to unfold the neutron spectra of various sources. The response functions act as the distribution of the neutrons that are recorded by the detector for each setup. The variation between unfolded spectra is not caused by the response functions but by the magnitude in the number of counts collected for each setup.

3.2 Testing the BSS

3.2.1 Experimental Setup

The LiI(Eu) detector was setup using the crank operated, steel, mobile storage unit, shown in Figure 26 [5]. The AmBe source was placed on the table, 30 cm from the detector. Using coaxial cables, the detector was attached to a CAEN data aquisition device that utilized the CoMPASS software to record the counts. This setup is used as it is fairly easy to repeat and requires the least amount of components, making it rather transportable. The collection occurred for approximately one hour for the bare, 2", 3", 5", 8", 10", and 12" sphere configurations, for a total of seven hours of data collection time. The data was recorded as counts per bin in SPE format per the CoMPASS software's capabilities. Using Python3, the counts for each setup were summed over the total number of bins. Next, the total counts were divided by the total run time of the detector, giving the counts per second for each detector setup.

The results were compiled in this manner because MAXED requires the counts per second for each detector setup to be combined into a single input file to conduct the spectrum unfolding.

Figure 26. Depiction of the BSS setup on the mobile storage unit. Reproduced with permission from [5].

3.2.2   MAXED Unfolding

The version of MAXED utilized for this research is part of the UMG package from RSICC, called MXD_FC33. There are three inputs required for MAXED to unfold a spectrum: the *.ibu measured data file, the *.fmt response functions file, and the *.flu default spectrum file. The format of these three files are particular to MAXED requirements. Each of the three file formats are listed and described in the following three tables [27].

The input file includes the measured data recorded by the LiI(Eu) for each setup. The format of this file is included in Table 1. An example input file is also shown in Figure 27. The first line is self-explanatory and is not used by MAXED. Line 2 is the number of measurements (7 for all sphere and bare setups) and the data correction factor. This value is set to zero so that the data is not changed. However, if the collection time was low, resulting in very few counts, the data correction factor

could be changed to a non-zero value to make-up for the lack of counts. However, this is not recommended because any anomalous counts will also be increases, which would then give inaccurate unfolding results. The rest of the lines are for the data for each configuration. Each of the inputs are separated by a space for these records. The identification for each setup cannot be more than 8-characters in length. Next, the diameter of the sphere is included in inches. The measured data is the corrected count rate. The measured data uncertainty is included in absolute units and then as a percentage. The default percentage values are used for this research. Lastly, a "flag" is included as an integer from one to seven. This includes the data in the unfolding. These records are repeated for all detector setups as additional lines. These records are summarized in Table 1.

```
AmBe Neutron Spectrum - 1 hr scans - T.Nichols - 12/10/2019
    7      0
Bare    0.0     7.580E-01     1.451E-02     1.914     6.71     1
2in     2.0     2.050E+00     2.386E-02     1.164     1.18     2
3in     3.0     5.546E+00     3.925E-02     0.708     1.08     3
5in     5.0     2.026E+01     7.118E-02     0.390     1.08     4
8in     8.0     2.908E+01     8.550E-02     0.325     1.08     5
10in    10.0    2.040E+01     7.150E-02     0.389     1.07     6
12in    12.0    1.909E+01     6.911E-02     0.402     1.07     7
```

Figure 27. Example MAXED input file for the measured data.

Table 1. The format for the measured data file input for MAXED [27].

Line Number	Description
1	A user chosen header (not used by MAXED; max 80 characters)
2	Number of measurements; Data correction factor (usually set to 0)
3a	Name for the bare setup; sphere's diameter (0"); measured data; absolute uncertainty; percentage uncertainty; a "flag" (a positive number for inclusion)
3b	Same as 3a but for the second setup (2" sphere)
...	...
Last	Same as 3a but for the last sphere (12")

The second input file includes the response functions. Once again, this file contains a header up to 80 characters long that is not used by MAXED. This file also includes a second header line with the same parameters as the previous one. The third line is the number of energy bin edges in the response function for the first setup and 0 for the units of energy (MeV). Next, the energy bin edges are listed. The dummy variables are set to 0 or to any other integer and are not used by MAXED. Additional lines are described in Table 2.

Table 2. The format for the response functions file input for MAXED [27].

Line Number	Description
1	A user chosen header (not used by MAXED; max 80 characters)
2	A user chosen header (not used by MAXED; max 80 characters)
3	Number of energy bin edges; units of energy (1 for MeV)
4	Energy bin edges
5	Dummy variable (set to 0)
6	Number of response functions
7a	Short response function ID; 2 blank spaces; long response function ID
7b	Dummy variable; response function units, six dummy variables
7c	Response functions for the designated setup
8a,8b,8c	Same as 7a, 7b, 7c for the next setup
...	...
Last	Same as 7a, 7b, 7c for the last setup (12" sphere)

The last input file is the default spectrum file. This includes the *a priori* spectrum information. Once again, the first line in this file is a user defined header of 80 characters or less that is not used by MAXED. The second record is the form of the a priori spectrum and the energy units. The form of the spectrum is set to 2, or fluence rate per bin. The units of energy is set to 1 for MeV. The first number in the third line is another dummy variable not used by MAXED. It is set to zero. The rest of the values in this line are the number of energy bins, repeated twice, and the highest

energy bin edge. The rest of the lines include the actual a priori spectrum data and are described in the Table 3 [27].

Table 3. The format for the *a priori* spectrum input file for MAXED [27].

Line Number	Description
1	A user chosen header (not used by MAXED; max 80 characters)
2	Default spectrum form; energy units
3	Dummy variable; number of energy bins (repeated); highest energy bin edge
4	First low energy bin edge; the first bin; uncertainty of the first bin
5	Second low energy bin edge; the second bin; uncertainty of the second bin
...	...
Last	Last low energy bin edge; the last bin; uncertainty of the last bin

After creating these three input files, MXD_FC33 is applied for the calculations. A control file can also be created but is not necessary to run the program. This involves listing the directory locations of each input file in a separate *.inp file. MXD_FC33 also requires the highest energy of the solution spectrum in the same units as the response functions, the user-requested final chi-squared per degree of freedom, the temperature and temperature reduction factor parameters, the energy bin structure and the representation of the solution spectrum, and the users choice of default spectrum scaling. The values chosen for this portion of research are included in Table 4. These values can are also included in the control file and are listed as separate lines.

For further information on how to create a control file, refer to the UMG package manual [27].

Table 4. Additional required values for MAXED to unfold. These values are also listed in the control input file [27].

Line Number	Chosen Values	Description
5	7.	Highest energy of the solution spectrum
6	1.1	Requested final chi-squared per degree of freedom
7	1.0, 0.85	Default temperature/temperature reduction factor parameters
8	2, 1	Energy bin structure of the default spectrum, solution spectrum is plotted as $\frac{df}{dE}$
9	0	Do not multiply the default spectrum with a scale factor
10	0	Do not use the MXD_FC33 determined scale factor

3.3 Nuclear Detonation Simulations in MCNP

Using the DTRA released weapon spectrum of Fat Man, MCNP models were created with various yields and heights-of-bursts (HOBs). Two models were created: a flat plain, and a flat plain with a single, 100 m tall concrete building. The building has one meter thick walls as well as a one meter thick base and ceiling. Additionally, the building is filled with the same air composition and density as the air outside of it. Schematics of the models are shown in Figures 28 and 29. The source probability (SP) and source information (SI) supply the probability distribution of neutrons emitted by the Fat Man source. These values are included in Appendix 0.4. These values set the probability distribution function of the source. The weighting factor relates the yield of the weapon to the neutron flux emitted. For Fat Man, the weighting factor is

1.590×10^{23} per kT of yield. The source position is set to 10 m, 200 m, and 1 km to model various HOBs. The detector is placed 1 km from the ground-equivalent of the source location (ground-zero). Using two F5 tallies, the neutron and photon flux is detected at a point detector and recorded in $particles/cm^2$ for a defined energy range of 0.01 eV to 20 MeV. The MCNP input card is also included in Appendix 0.4.
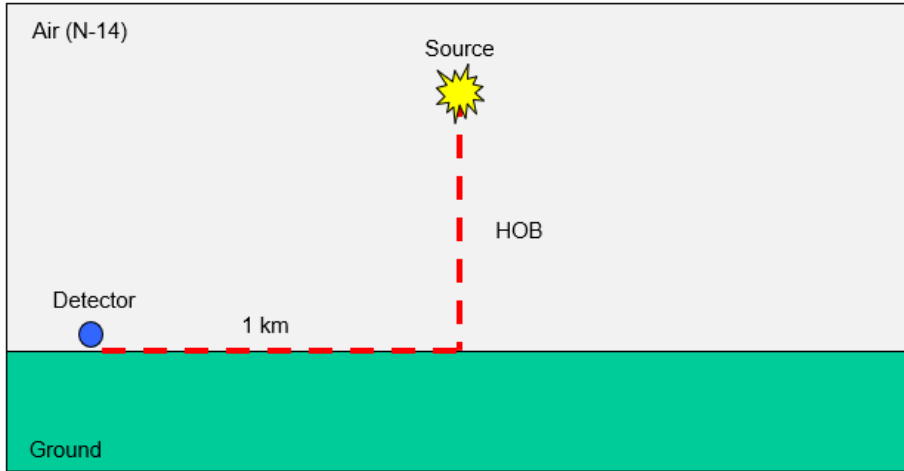
Figure 28. Schematic of the flat plain model in MCNP.
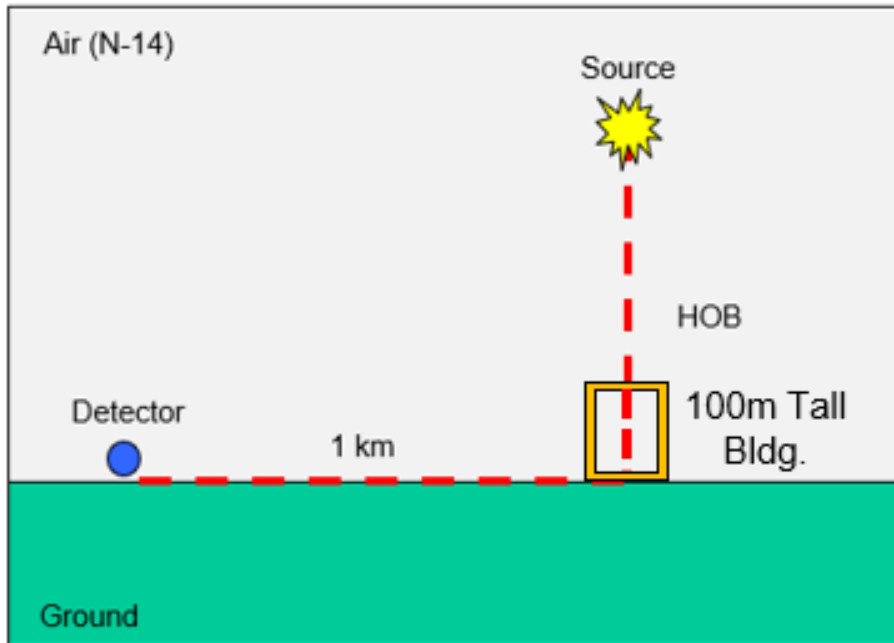
Figure 29. Schematic of the single building on a flat plain model in MCNP.

The goal of modeling nuclear detonations in MCNP is to provide an estimate of the radiation that would be incident on a solar panel located approximately 1 km away from a NW explosion. Although, realistically, solar panels at this range are likely to be damaged by the shock wave, the signal resulting from radiation interactions in the solar panels will potentially be transmitted to a control facility a substantial distance away before the panels are destroyed. A distance of 1 km is a good starting point to examine the fluxes emitted by a detonation of various yields. It should be noted that weapons with smaller yields may not have a strong enough output that would reach a panel 1 km away. On the other hand, weapons with much higher yields will likely destroy the panel before any information could be collected. Additionally, a radius of 1 km is approximately one-fourth the size of a medium-sized city like Dayton, Ohio. At this range, it is likely that the radiation will interact with at least one solar panel in Dayton or any arbitrary city.

IV. Results and Analysis

The purpose of this section is to show the collective results of the research conducted. This includes the results from the BSS testing, the AmBe unfolding, and the MCNP scenario modeling. The AmBe unfolded spectrum is compared to the ISO 8529 reference spectrum to show the validity of MAXED's deconvolution [28]. The BSS collected data is compared to the results of the BSS MCNP model to show the accuracy of the BSS and to validate that MCNP accurately models complex scenarios. Additionally, the results of the MCNP detonation scenarios are discussed.

4.1 BSS Counting Results

The raw data collected by the BSS includes the counts for all events occurring in the LiI(Eu) detector. Shown in Figure 30, the photopeaks correspond to the characteristic neutron events. However, the additional low-energy events are likely caused by gammas interacting with the detector. Since this research focuses on neutrons, the low-energy events are excluded from the AmBe unfolding. The varying heights in the peaks are characteristic of the neutron moderation occurring in the different sized polyethylene spheres.
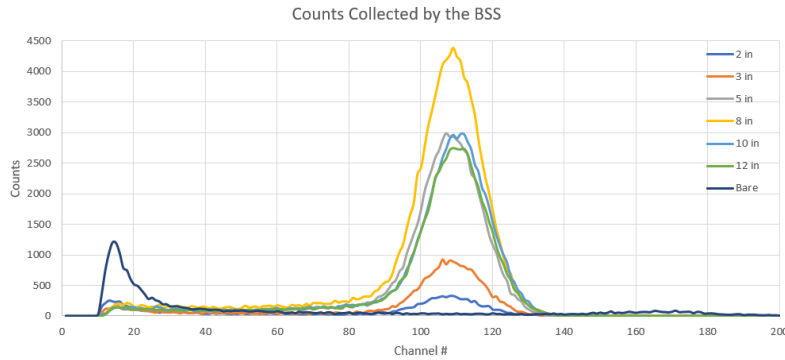
Figure 30. Raw counts collected by the BSS for one hour runs.

The five and 10-inch spheres have nearly identical peak values near 3,000 counts.

Whereas, the 12-inch sphere peaks with a magnitude of approximately 250 counts less than the five and 10-inch peaks. Additionally, the eight-inch sphere has the highest peak value at just below 4,500 counts. Furthermore, the two smallest spheres, the two and three-inch spheres, have the lowest magnitude peak values at around 300 and 900 counts, respectfully.

These distinguishing characteristics can be explained by examining the response matrix of the BSS. As shown in the response matrix, Figure 23, the two and three-inch spheres have the lowest responses for higher energy neutrons and the highest responses for low energy neutrons. The low counts associated with the smaller spheres are physically justified by the examining the known AmBe neutron spectrum and the response matrix of the detector. Since most of the neutrons emitted by the AmBe are around 4 MeV, a majority of the neutrons will not be moderated sufficiently by two or three inches of polyethylene and will likely pass through the detector, uncollected. However, there is still a chance that the emitted neutrons scatter before reaching the polyethylene sphere since air is present between the source and detector. If the neutrons scatter sufficiently, their energies will be low enough to be collected by the detector. This is the most probable cause of counts collected for the two and three-inch spheres.

The counts of the five and 10-inch spheres can also be explained by their corresponding response functions. The response function of the five-inch sphere peaks around 0.6 MeV. However, this sphere has the highest response of all spheres from 2 keV to 0.6 MeV. On the contrary, the response of the 10-inch sphere only surpasses the response of the five-inch sphere for neutron energies above 2 MeV. For all energies below this threshold, the response of the 10-inch sphere is an order of magnitude lower than that of the five-inch sphere. The most likely cause of the similar counts for these two spheres is that the neutrons reaching the spheres, on average, have energies

of 2 MeV or greater. For this reason, the 10-inch sphere moderates and records most of these neutrons. The five-inch sphere, however, only moderates and records some of them. The rest simply pass through the detector without getting recorded. The five-inch sphere is also moderating and recording a significant amount of the neutrons with energies below 2 MeV, whereas the 10-inch sphere does not due to a high likelihood of the polyethylene absorbing the neutrons before they reach the detector. When adding the described events for each sphere, the ratio between the two spheres is roughly the same, leading to two peaks with nearly the same counts.

The same explanation applied to the 10-inch sphere can be applied to the 12-inch sphere. The slight decrease in counts is likely caused by an increase of neutron absorption in the polyethylene sphere or an increase in neutron deflection away from the detector. This is also reflected in the response function by a slight decrease in magnitude of the peak response for the 12-inch sphere compared to the magnitudes of the eight and 10-inch response peaks.

Lastly, the eight-inch sphere has the highest counts of all setups. The most plausible cause of this is that most of the neutrons have an energy of approximately 2 MeV when they reach the polyethylene spheres, which corresponds to the peak response of the eight-inch sphere. In fact, the eight-inch sphere has the highest response for 2 MeV neutrons. Additionally, the eight-inch sphere has a higher response for lower energy ranges than the 10 and 12-inch spheres. Therefore, the eight-inch sphere is recording more lower-energy neutrons than the two larger spheres. This will also inflate the number of counts being recorded, leading to an increase in peak magnitude.

Finally, the counts were summed for the photopeaks only. From there, the count rate is determined for each sphere including the bare detector. The uncertainties are calculated according to the steps described below [23]. First, the absolute uncertainty, σ, is determined for each detection configuration according to Equation 17, where $\overline{x}$

is the sample mean and n is the sample size.

$$\sigma = \sqrt{\frac{\sum (x - \overline{x})^2}{n}} \tag{17}$$

Next, the fractional uncertainty of the count rate, CR_{frac}, is calculated using Equation 18, where N is the total number of counts under the photopeak. The values for this are between 0.3% and 1.2% for the setups involving moderating spheres. The bare detector has a fractional uncertainty closer to 2%. This is likely due to the reduced amount of interactions in the detector as a results of the high energy of the incident neutrons as compared to the lower energy of the moderated neutrons, leading to a significant decrease in the number of counts recorded compared to those recorded for the other setups.

$$CR_{frac} = \frac{1}{\sqrt{N}} \tag{18}$$

Then, the absolute uncertainty of the count rate is calculated by multiplying the fractional uncertainty by the count rate for the respective detector setup. Finally, the R-value, a measure of experimental error, is calculated using Equation 19. Once again, these values are fairly low for the setups involving the polyethylene spheres (around 1%), however it is significantly higher for the bare setup (6.71%). This high error can again be explained by the low counts. All of the values described are included in Table 5, where the count rate (CR) units are *counts/second*. The CR, CR_{frac}, CR_{abs}, and R values are then used by MAXED to unfold the AmBe spectrum.

$$R = \frac{2(\sigma)}{N} \tag{19}$$

Table 5. **The associated uncertainties calculated for each sphere presented in the format for the measured data file input for MAXED [27].**

Detector	N	σ	CR	$CR_{frac}(\%)$	CR_{abs}	R (%)
Bare	2729	91.57	7.580E-01	1.914	1.451E-02	6.71
2in	7381	43.57	2.050E+00	1.164	2.386E-02	1.18
3in	19967	107.43	5.546E+00	0.708	3.925E-02	1.08
5in	65659	353.86	2.026E+01	0.390	7.118E-02	1.08
8in	94731	510.60	2.908E+01	0.325	8.550E-02	1.08
10in	66249	353.75	2.040E+01	0.389	7.150E-02	1.07
12in	61908	330.79	1.909E+01	0.402	6.911E-02	1.07

4.2 AmBe Unfolding Results

Using Python, the unfolded AmBe neutron spectrum and the scaled reference spectrum are plotted. The spectra are shown in Figures 31. The reference ISO8529 spectrum was scaled by a factor of 245 for the best fit. Additionally, the first energy bin is excluded due to having an uncharacteristically high value of 805 $particles/cm^2$. This is likely caused by a binning error with MAXED and for this reason the corresponding bin of 0.1067 MeV is treated as an outlier and is excluded from the results. It is important to note that MAXED returned a final chi-squared value was exceptionally high because of this, with a value of 1,022.593 for this unfolding. For this reason, the chi-squared statistic is not an accurate representation of the closeness of fit between the *a priori* spectrum and the unfolded spectrum.
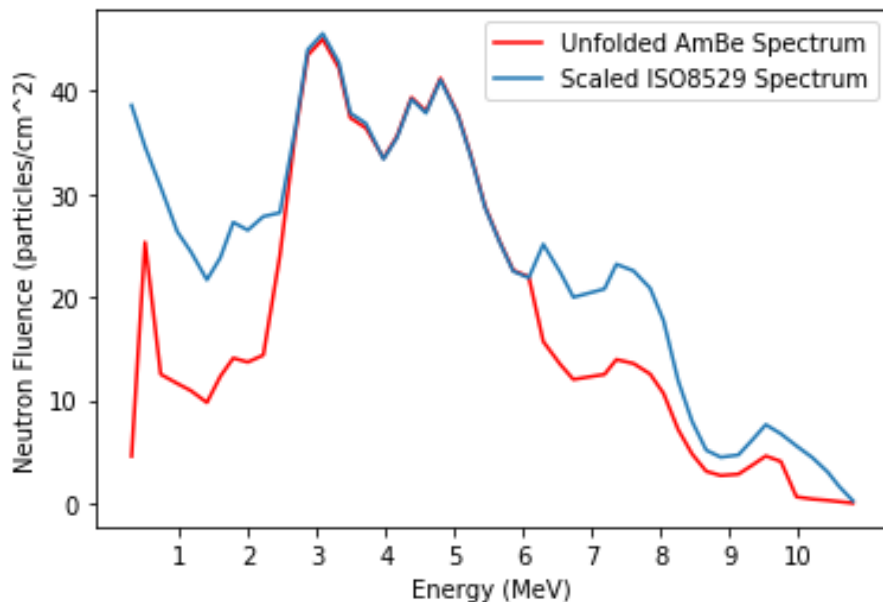
Figure 31. Resulting AmBe neutron unfolded spectrum and scaled ISO8529 reference spectrum.

The two spectra have similar characteristics, with respect to the size of the peaks. The two main peaks of the unfolded spectra occur around 3.1 and 4.7 MeV, corresponding to the peak energies of the ISO 8529 spectrum. However, there are slight deviations between the unfolded spectrum and the reference spectrum. For example, the flux below 3 MeV of the unfolded spectrum is significantly lower than the scaled reference spectrum. The likely cause for this discrepancy is statistical variations in MAXED's unfolding for the lower energy region. For lower energies, the interactions of the neutrons are harder to predict. This is because neutrons are more likely to be absorbed by the polyethylene or even the detector at lower energies, resulting in indistinguishable capture reactions. On the other hand, the number of scatterings in the polyethylene varies widely. The combination of these events leads to a large fluctuation in MAXED's interpretation of what is happening to the lower energy neutrons. Additionally, the unfolded spectrum flux for energies above approximately 6 MeV is also lower than the ISO8529 spectrum flux. The most probable cause of this

53

discrepancy is thermalization due to the environment around the detector. However, it is also likely that there are events occurring in the detector that are not caused by neutrons. Although most of the low-energy events are excluded, it is possible that there are gammas interacting with the detector and being counted as neutrons with energies similar to those that make up the photopeaks discussed in Figure 30. This would include the counts of these non-neutron events in the MAXED unfolding, and possibly skew the results.

To assure the accuracy of MAXED's unfolding process, a model of the experiment with the bare LiI(Eu) detector was created in MCNP where the neutron source is set to equal the neutron energy distribution provided by the ISO8529 source. The MCNP input deck for this model is included in the appendix. A schematic of the model setup is included in Figure 32. The neutron flux averaged over the LiI(Eu) detector cylinder was calculated in this model to show the theoretical neutron spectrum after the neutrons traversed 30 cm in air in a room with surrounding concrete walls. This gives a more accurate view of the neutron energies that are reaching the detector rather than assuming that the *a priori* spectrum is the exact same as the ISO8529 AmBe spectrum. The resulting spectrum produced by the model is shown scaled in Figure 33 with the scaled ISO8529 spectrum. The scaling factor for the ISO8529 spectrum is the same and the MCNP modelled spectrum is scaled by a factor of 2.88×10^7.
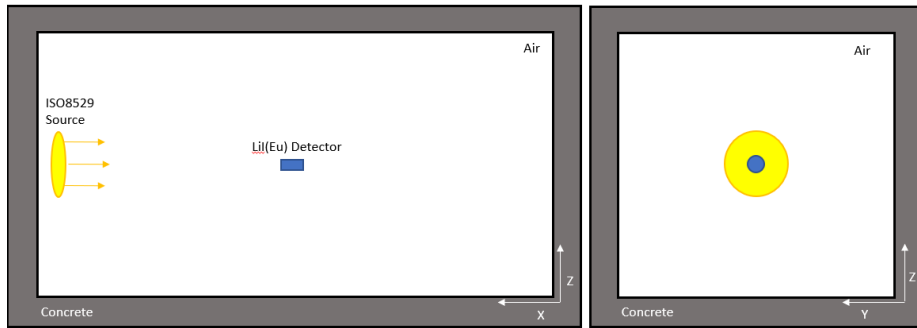
Figure 32. Schematic showing the setup of the MCNP model of the ISO8529 source neutron spectrum.
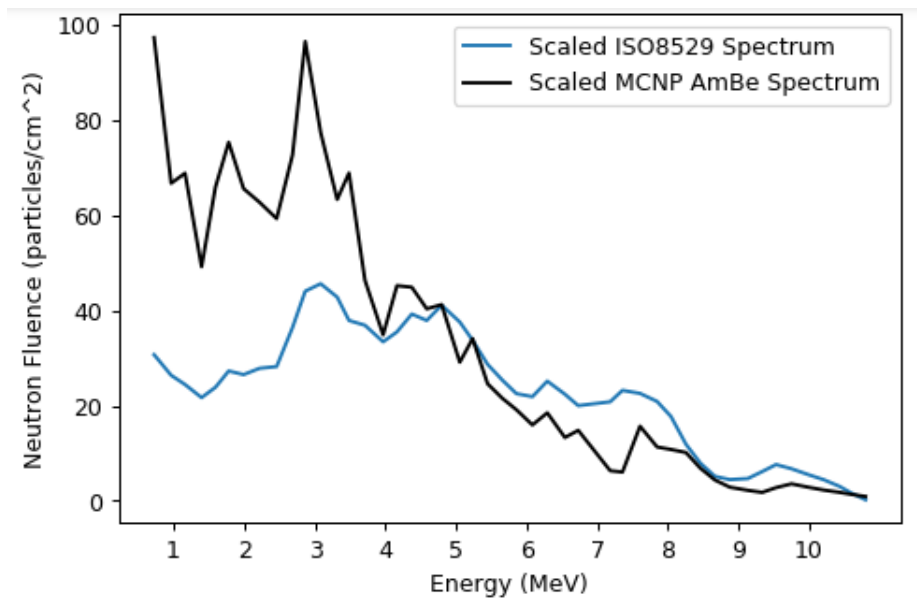
Figure 33. Scaled neutron spectrum resulting from the MCNP model of the moderated ISO8529 source with the scaled ISO8529 source spectrum.

As shown, the scaled MCNP AmBe spectrum varies from the ISO8529 spectrum. This is because the model accounts for any thermalization as a result of interactions with the environment. In this case, the environment consists of concrete walls and air around the source and detector. Regardless, this slight moderation was likely not accounted for with the ISO8529 source since these spectra are typically recorded in highly controlled environments where the scattering is minimized. The slight deviations between the two spectra, expressed by the overall shape of the spectra, can

be explained by the lack in accuracy to the realistic dimensions of the experimental setup. A smaller version of the concrete room was modeled in MCNP rather than an accurate replica as the complexity of the model would increase significantly, and with it, the overall computer run time. This includes the exclusion of the wooden table that the AmBe source was resting on.

Using the MCNP modelled spectrum as the new, more accurate *a priori* spectrum, MAXED was utilized again to unfold the AmBe neutron spectrum. The resulting unfolded spectrum is shown in Figure 34 along with the scaled MCNP modelled spectrum. Again, MAXED unfolded an uncharacteristically high fluence to the first few energy bins. In this case, it is likely caused by the high fluence associated with the modelled spectrum. For this reason, the first three bins are excluded from the results and the characteristic unfolded and modelled spectrum is plotted as shown in Figure 35. As shown, the new unfolded AmBe spectrum is fairly consistent with the MCNP modelled spectrum after 4 MeV. However, there is a large difference between the spectra for energies below this threshold. This is likely caused by the absorption of neutrons below 4 MeV by the environment that was not modelled in MCNP in addition to the low-energy statistical discrepancies discussed previously. It should be noted that because of this error in the first few energy bins, the chi-squared value returned by MAXED for this unfolding was 40.073, which is significantly lower than chi-squared returned for the first unfolding due to the high fluence of the MCNP modelled spectrum for the first three energy bins. This is indicative of MAXED's reliance on the accuracy of the *a priori* spectrum: the more accurate the *a priori* spectrum, the better the unfolding. Logically, this makes sense as MAXED depends on the *a priori* spectrum to initiate the unfolding process mathematically. However, this also indicates that the chi-squared value, or MAXED's way of stating the goodness-of-fit, is also dependent on the accuracy of the *a priori* spectrum. As a result, the viability

of utilizing MAXED to unfold known and unknown neutron spectra relies heavily on the competency of the user. Shown in Figure 36, both unfolded AmBe spectra are plotted to show the difference in MAXED's unfolding results by using two slightly different *a priori* spectra.
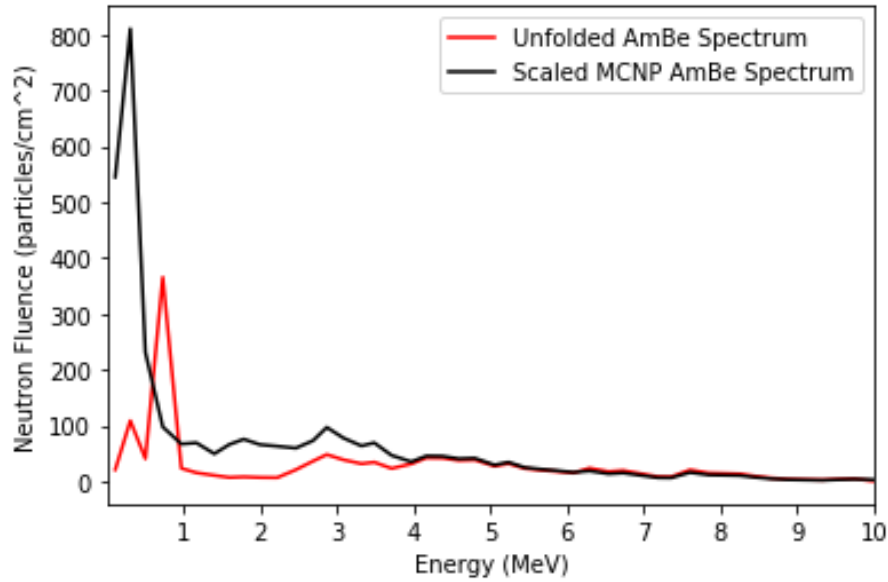
Figure 34. Neutron spectra resulting from the MAXED unfolding of the BSS data with the MCNP modelled spectrum as the *a priori* spectrum and the scaled MCNP modelled spectrum.
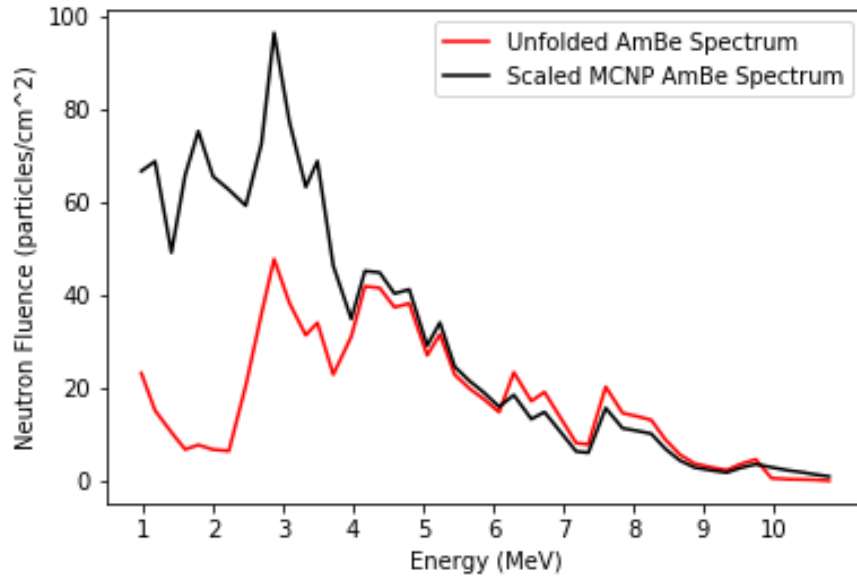
Figure 35. Neutron spectra resulting from the MAXED unfolding of the BSS data with the MCNP modelled spectrum as the *a priori* spectrum and the scaled MCNP modelled spectrum excluding the first three energy bins.
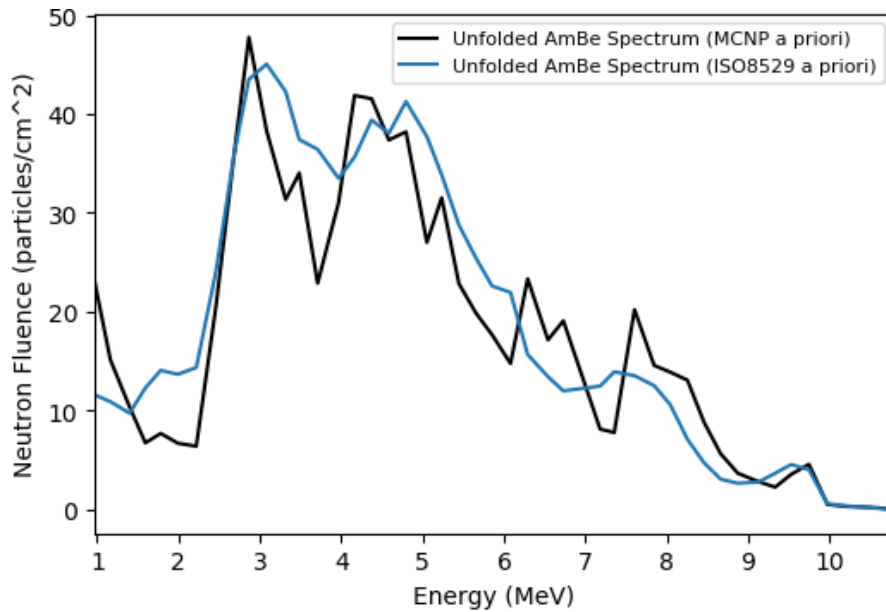
Figure 36. Neutron spectra resulting from the MAXED unfolding of the BSS data with the MCNP modelled spectrum as the *a priori* spectrum and the ISO8529 spectrum as the *a priori.*

4.3 MCNP Scenario Modeling Results

For three different yields and three different HOBs, the neutron and photon fluxes are found at a point 1 km away from the ground equivalent detonation site (ground-zero) in MCNP. The fluxes for the 1 kT yield models are plotted and shown in Figures 37 through 44. The only difference between the 1 kT yield models and the 10 kT and 100 kT models is an increase to the both the neutron and gamma fluxes by an order of magnitude. This is because MCNP does not treat the different yields as anything other than a weighting factor. This essentially multiplies the generated flux by a user-designated factor. Since this research utilized the DTRA released spectra, it also uses the corresponding weighting factor of 1.590×10^{23} per kT yield. The higher yield fluxes are included in the appendix. For both the plain and the single building model, the resulting neutron and photon fluxes are the same for all yields at 1 km HOB. Since the 100 m tall concrete building is directly beneath the source location, the neutrons that reach the detector do not interact with the concrete building. This is a matter of simple geometry. If the building was placed more in-line with the trajectory of neutrons reaching the detector, the neutron flux would be slightly lower due to interaction with the concrete, as shown in the 200 m HOB model.

Figure 37. Neutron and photon flux for the flat plain model with 1 kT yield and 1 km HOB.
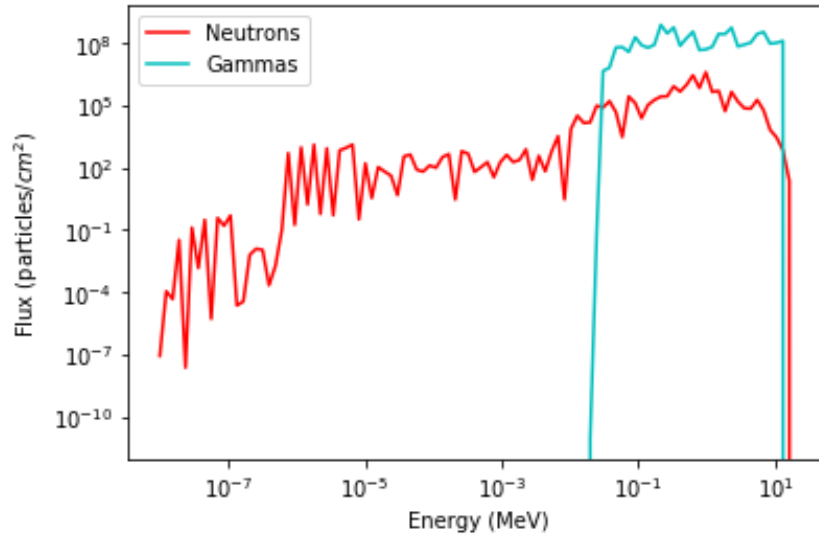
Figure 38. Neutron and photon flux for the single building model with 1 kT yield and 1 km HOB.

Since the source is set to only emit neutrons, the production of gamma's is a result of interactions with the nitrogen-14 air. Although the (n,γ) absorption cross-section for ^{14}N is fairly small, as shown in Figure 39, it is still occurring on some level [19]. Via the process shown in Equation 20, the neutron is absorbed by the ^{14}N nucleus which then emits a γ-ray and ^{15}N. Although the probability is even less

than the previous reaction, the ^{15}N nucleus may absorb another neutron to form ^{16}N, as shown in Equation 21. This reaction is important because it forms the unstable isotope ^{16}N, which is known to β decay and simultaneously release a γ-ray, usually with an energy of 6.130 MeV [29]. The MCNP output also credits the generation of photons to Bremsstrahlung radiation, proton annihilation, and pair production but at an order of magnitude or more less than those created due to neutron capture.
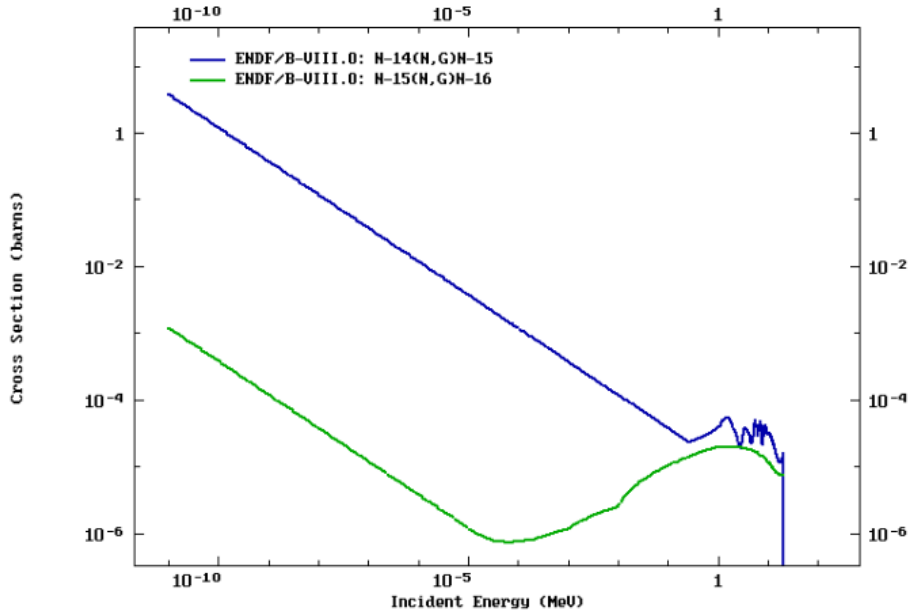
Figure 39. Neutron absorption cross-sections for ^{14}N and ^{15}N [19].

$$^{14}N + {}^{1}n \rightarrow {}^{15}N + \gamma \tag{20}$$

$$^{15}N + {}^{1}n \rightarrow {}^{16}N + \gamma \tag{21}$$

At a HOB of 200 km, there is a slight difference in the neutron fluxes for the flat plain and the single building models with an additional peak around 10^{-7} MeV. This is likely due to the minimal interactions that some neutrons have with the concrete building. A relatively small amount of the neutrons are being moderated by the

concrete before reaching the detector, resulting in an increase of slow neutron flux by approximately 10^5 particles/cm^2. The reason that this value is so small is, again, a matter of geometry. Although 200 m is significantly closer to the top of the 100 m tall building than the 1 km HOB, the trajectory of the majority of neutrons reaching the detector is not interacting with the concrete building.
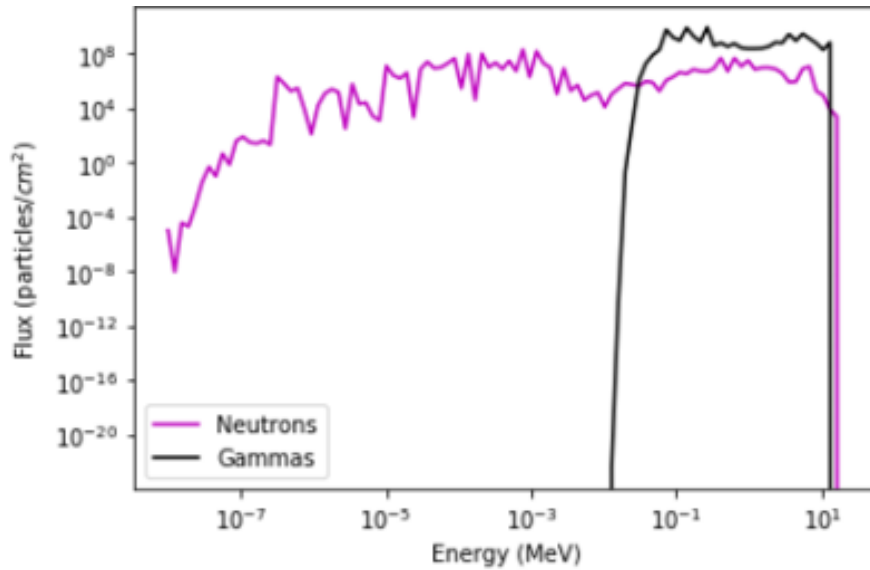
Figure 40. Neutron and photon flux for the flat plain model with 1 kT yield and 200 m HOB.
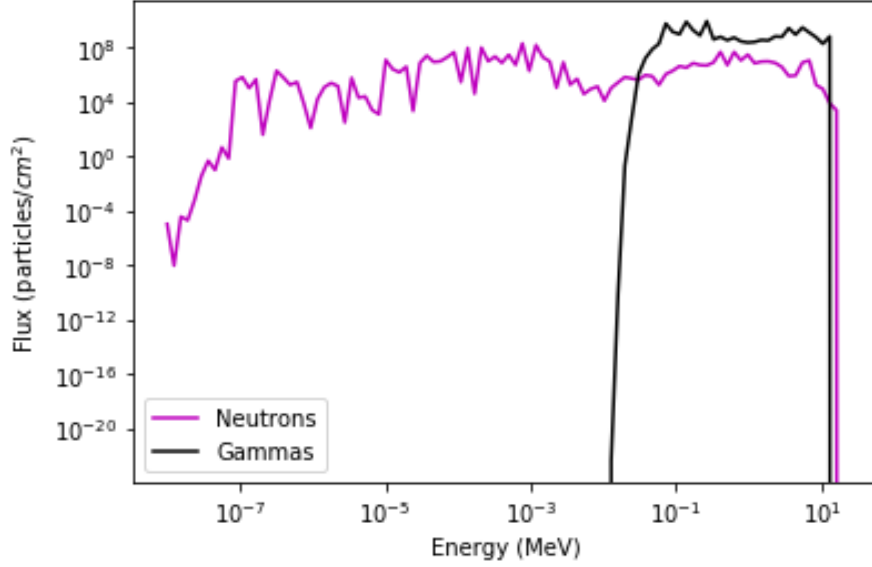
Figure 41. Neutron and photon flux for the single building model with 1 kT yield and 200 m HOB.

Finally, at a HOB of 10 m, the neutron source or detonation occurs inside of the concrete building for the single building model. This results in a dramatic difference between the flat plain and the single building model spectra, as shown in Figures 43 and 44. Most of the slow neutrons do not reach the detector when originating inside of the building, resulting in a 10 order of magnitude reduction in the neutron flux in this region. There is also a significant difference in the photon flux: the photon flux goes from 10^9 particles/cm^2 for the flat plain model to nearly 10^7 particles/cm^2 between 0.01 and 0.2 MeV for the single building model. However, after 0.2 MeV, the photon flux increases to approximately 10^9. This is likely due to the lower energy photons being absorbed by the concrete, whereas the higher energy photons pass through the building. Once again, the MCNP output credits this production of photons to the (n,γ) capture reactions. In addition to the neutron captures occurring in the Nitrogen-14 air, there are additional neutron captures occurring in the concrete of the building. In particular, the Silicon-28 and Oxygen-16 that make-up approximately 87% of the concrete are reacting via neutron capture according to Equations 22 and

63

23 to produce γ-rays. Although the (n,γ) absorption cross-sections are fairly low, as shown in Figure 42, they are still occurring in the material due to the large amount of generated neutrons emitted by the source.

$$^{16}O + \; ^1n \; \rightarrow \; ^{17}O + \; \gamma \tag{22}$$

$$^{28}Si + \; ^1n \; \rightarrow \; ^{29}Si + \; \gamma \tag{23}$$

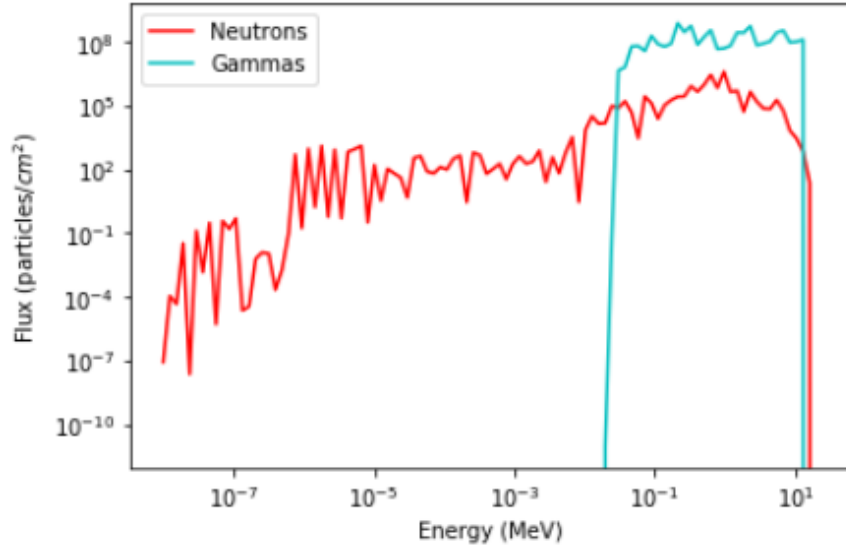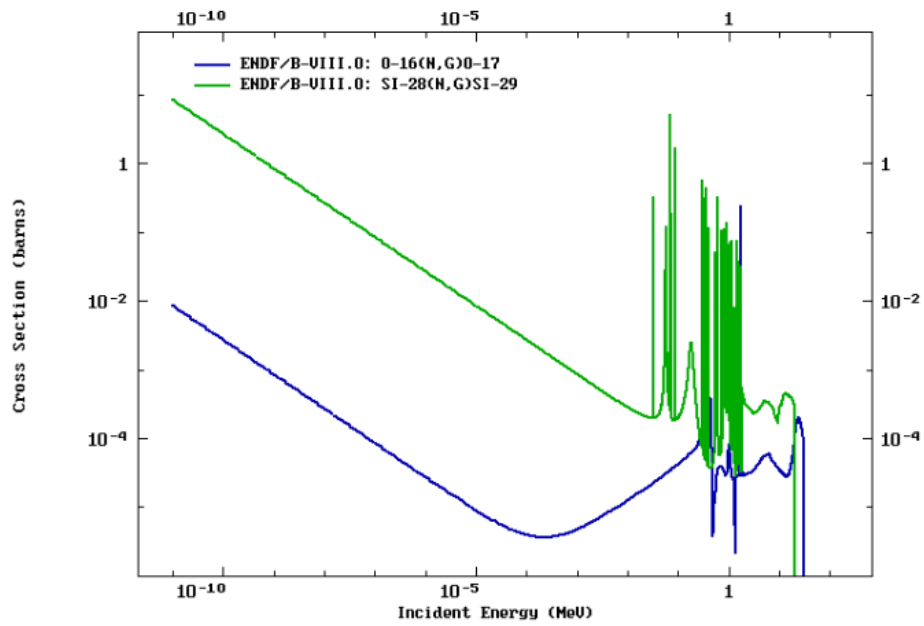Figure 42. Neutron absorption cross-sections for Si-28 and O-16.
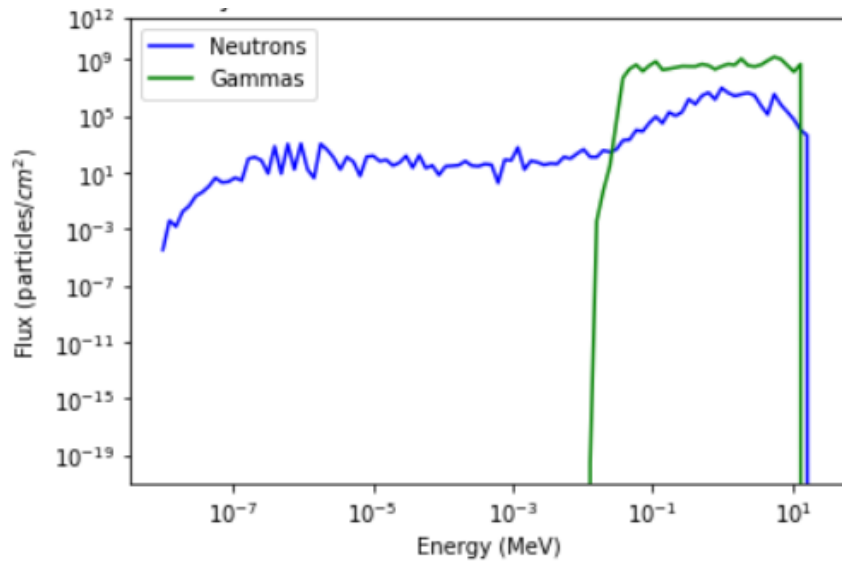
Figure 43. Neutron and photon flux for the flat plain model with 1 kT yield and 10 m HOB.
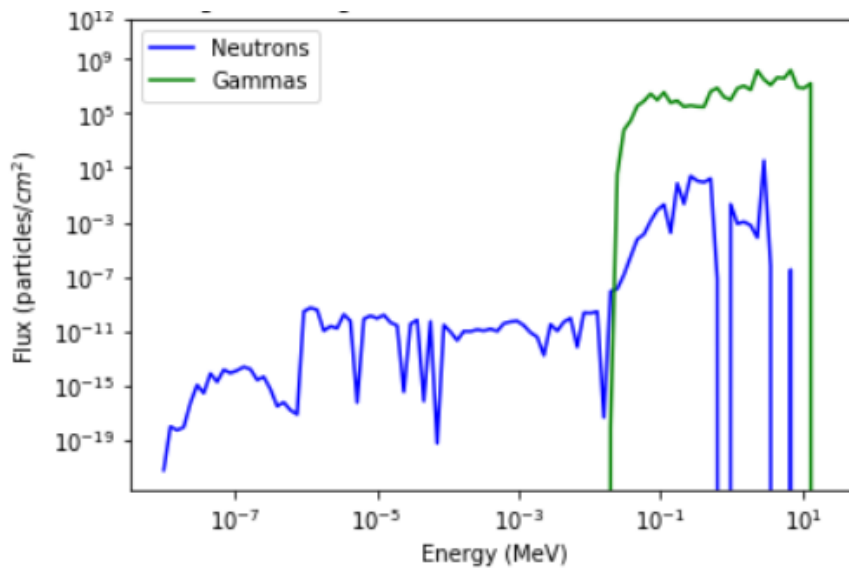
Figure 44. Neutron and photon flux for the single building model with 1 kT yield and 10 m HOB.

65

V. Conclusion and Future Work

This chapter reviews the main topics of the previous chapters and concludes the research conducted for this thesis. Additionally, the work conducted for this thesis is connected to the over-arching DTRA project as a whole. Future work including where the project is headed is also discussed.

5.1 Conclusion

By utilizing the unfolding program Maximum Entropy Deconvolution (MAXED) with the Bonner Sphere Spectrometer (BSS), the neutron spectrum of various sources can be characterized. When used to unfold an americium-beryllium (AmBe) neutron source, the resulting spectrum showed similar characteristics to the ISO8529 reference AmBe spectrum with two peaks around 3.1 and 4.7 MeV. There are slight deviations between the unfolded spectrum and the reference spectrum, which is likely the cause of the high chi-squared value. One of the deviations is the slight decrease in the high energy neutron flux. This difference is likely caused by thermalization through interactions with the environment around the detector and the source. Additionally, there are slight deviations in the low energy region. These may be caused by low-energy events that are not caused by neutron interactions as well as statistical variations in MAXED's unfolding.

The MCNP model of the BSS experimental setup was developed to test these theories and to verify the accuracy of MAXED and its unfolding process. The resulting, modelled neutron spectrum shows the effects of neutron moderation via interactions with the air and concrete walls surrounding the detector and source. Thus, the model gives a more accurate representation of the ISO8529 spectrum particularly for this experiment since the true ISO8529 spectrum was determined in a more controlled

environment. By using this spectrum as the *a priori* spectrum, MAXED can conduct a more accurate neutron spectrum unfolding of the AFIT AmBe source. The resulting, unfolded spectrum was found to statistically be a better fit to the true spectrum of the AmBe source, as shown in the resulting lower chi-squared value of 39.439. Additionally, the magnitudes of the corresponding peaks were closer in value to the scales ISO8529 spectrum. This indicated that the neutron spectrum of the AFIT AmBe source is likely very close to the ISO8529 AmBe spectrum, although they are not identical. This also provided insight into the MAXED unfolding process by indicating its reliance on the accuracy of the *a priori* spectrum. This puts a large dependence on the competency of the user and their ability to produce an accurate guess spectrum either conceptually or via modeling.

The neutron and photon fluxes from both the flat plain and the single building environments were modeled with MCNP for various height-of-bursts (HOBs) and yields. The resulting fluxes are consistent with the physics of neutron interactions. Neutron moderation is observed through an increase in the lower-energy neutron flux for the single building model at 200 m HOB. Absorption is visible in the significant neutron flux decrease for the single building model at 10 m HOB. An increase in the gamma flux reflects the neutron, gamma reactions in the concrete. All of which are consistent with the interactions detailed in previous chapters

In conclusion, the methodology followed in this research can be applied to other, unknown neutron sources, specifically the Fast Beam Facility (FBF) at The Ohio State University Nuclear Reactor Laboratory (OSU-NRL). The BSS coupled with the program MAXED is a viable technology in detecting and characterizing both known and unknown sources.

5.2 Future Work

To further the long-term goal of studying photovoltaics response to nuclear detonations, additional work can be conducted. First, the neutron beam measurements for the FBF at OSU-NRL can be conducted using the BSS and the resulting spectrum can be unfolded with MAXED. This will be done by taking the BSS and the required power and collection technology to OSU-NRL when the construction of the FBF is completed. From here, the BSS will be setup directly against the FBF beam port. The reactor will be powered on, likely to its maximum power of 450 kW, and the neutron counts will be collected for each detector sphere setup, including one for the bare detector. Since the flux coming from the reactor is significantly larger than the neutron flux emitted by an AmBe source, it is likely that each detection setup will only have to be irradiated for a short period of time (tens of minutes maximum). From this data, the unfolded spectrum can be determined using MAXED, where the *a priori* spectrum is modeled using MCNP. This unfolded spectrum will then be compared to the weapon detonation scenario models spectra. Additionally, more detailed weapon detonation models can be constructed in SWORD for a more accurate weapon spectra. All of this additional research combined will provide a better understanding of what the FBF neutron spectrum should look like in order to mimic the neutron spectrum of a nuclear weapon detonation. This will most accurately simulate the response of the photovoltaics in a real nuclear detonation scenario.

Appendix A. AmBe Sample Input Files

AmBe Control File

```
AmBeInput1hr.ibu                         File with measured data 1 hr
AmBeRFA11.fmt                            File with response functions (RF)
AmBeOut10                                Name of output file
MCNPAmBeSpectrum.flu                     File with default spectrum (DS)
11.                                      Highest energy (use energy units of RF)
1.1                                      requested final CHI^2 P.D.F.
1.0,0.85                                 temperature, temp. reduction fact.
2,1                                      2 = use the DS energy bins, 1 = dF/dE
0                                        1 = scale DS
0                                        0 = use the MAXED DS scale factor
```

AmBe Raw Data File

```
AmBe Neutron Spectrum - 1 hr scans - T.Nichols - 12/10/2019
    7    0
Bare    0.0     7.580E-01     1.451E-02     1.914     6.71     1
2in     2.0     2.050E+00     2.386E-02     1.164     1.18     2
3in     3.0     5.546E+00     3.925E-02     0.708     1.08     3
5in     5.0     2.026E+01     7.118E-02     0.390     1.08     4
8in     8.0     2.908E+01     8.550E-02     0.325     1.08     5
10in    10.0    2.040E+01     7.150E-02     0.389     1.07     6
12in    12.0    1.909E+01     6.911E-02     0.402     1.07     7
```

AmBe Response Functions File

```
        DECEMBER-18-2019 RESPONSE FUNCTION FOR AMBE UNFOLDING
Neutron Response Functions for BS, units: cm^2, pSv, pSv cm^2
        29   1
 1.000E-11 1.000E-08 2.512E-08 6.310E-08 1.000E-07 2.512E-07 1.000E-06 1.000E-05
 1.000E-04 1.000E-03 1.000E-02 2.512E-02 3.981E-02 5.248E-02 6.310E-02 1.000E-01
 1.067E-01 1.585E-01 2.512E-01 3.981E-01 6.310E-01 1.000E+00 1.585E+00 2.512E+00
 3.981E+00 6.310E+00 1.000E+01 1.585E+01 2.512E+01
        0
        7.000E+00
Bare
 1.000E+00        cm^2          0          0    3    1    1    0
 7.304E-02 7.225E-02 6.984E-02 6.759E-02 6.018E-02 4.373E-02 1.875E-02 6.583E-03
 2.150E-03 6.941E-04 4.496E-04 3.573E-04 3.318E-04 3.151E-04 2.965E-04 3.058E-04
 4.148E-04 1.384E-03 2.666E-04 1.401E-04 1.104E-04 1.019E-04 9.015E-05 5.172E-05
 3.079E-05 1.900E-05 1.222E-05 8.765E-06
2in
 1.000E+00        cm^2          0          0    3    1    1    0
 3.991E-02 5.050E-02 6.780E-02 8.087E-02 9.975E-02 1.135E-01 1.014E-01 7.580E-02
 5.157E-02 3.368E-02 2.820E-02 2.499E-02 2.419E-02 2.254E-02 1.973E-02 1.871E-02
 1.615E-02 1.409E-02 1.078E-02 7.548E-02 5.143E-03 3.421E-03 2.030E-03 1.210E-03
 7.411E-04 3.641E-04 2.423E-04 1.221E-04
3in
 1.000E+00        cm^2          0          0    3    1    1    0
 3.012E-02 3.794E-02 4.991E-02 6.296E-02 8.380E-02 1.120E-01 1.264E-01 1.202E-01
 1.037E-01 8.647E-02 7.946E-02 7.477E-02 7.354E-02 7.342E-02 6.860E-02 6.743E-02
 6.456E-02 5.806E-02 4.859E-02 4.203E-02 3.116E-02 2.253E-02 1.484E-02 9.301E-03
 5.840E-03 3.280E-03 2.130E-03 9.868 E-04
5in
 1.000E+00        cm^2          0          0    3    1    1    0
 1.447E-02 1.885E-02 2.428E-02 3.081E-02 4.111E-02 5.834E-02 7.984E-02 9.106E-02
 9.682E-02 1.026E-01 1.064E-01 1.061E-01 1.088E-01 1.101E-01 1.112E-01 1.124E-01
 1.166E-01 1.179E-01 1.221E-01 1.169E-01 1.075E-01 9.487E-02 7.279E-02 5.242E-02
 3.795E-02 2.215E-02 1.626E-02 8.035E-03
8in
 1.000E+00        cm^2          0          0    3    1    1    0
 3.910E-03 4.877E-03 6.675E-03 7.855E-03 1.067E-02 1.534E-02 2.166E-02 2.648E-02
 3.096E-02 3.709E-02 4.137E-02 4.315E-02 4.572E-02 4.762E-02 5.167E-02 5.302E-02
 5.948E-02 6.963E-02 8.384E-02 9.917E-02 1.136E-01 1.195E-01 1.163E-01 9.952E-02
 8.168E-02 5.671E-02 4.324E-02 2.547E-02
10in
 1.000E+00        cm^2          0          0    3    1    1    0
 1.502E-03 1.758E-03 2.458E-03 3.018E-03 4.149E-03 5.836E-03 8.158E-03 1.017E-02
 1.199E-02 1.478E-02 1.649E-02 1.736E-02 1.841E-02 1.913E-02 2.177E-02 2.239E-02
 2.587E-02 3.240E-02 4.273E-02 5.746E-02 7.585E-02 9.371E-02 1.038E-01 9.738E-02
 8.754E-02 6.881E-02 5.527E-02 3.512E-02
12in
 1.000E+00        cm^2          0          0    3    1    1    0
 5.404E-04 6.394E-04 9.201E-04 1.124E-03 1.528E-03 2.141E-03 2.864E-03 3.688E-03
 4.442E-03 5.333E-03 5.952E-03 6.398E-03 6.845E-03 7.151E-03 8.159E-03 9.989E-03
 9.989E-03 1.306E-02 1.857E-02 2.758E-02 4.223E-02 6.138E-02 7.817E-02 8.313E-02
 8.291E-02 7.392E-02 6.023E-02 3.969E-02
```

AmBe Default Spectrum File

```
AmBe Default Spectrum - MCNP Modeled AmBe Spectrum
        1              1                        fluence rate per bin, Energy units MeV
        1             49          49   10.796
  0.1067 3.03E+00 3.03E+00
  0.3031 4.50E+00 4.50E+00
  0.4998 1.28E+00 1.28E+00
  0.7266 5.41E-01 5.41E-01
  0.9685 3.71E-01 3.71E-01
  1.1648 3.82E-01 3.82E-01
  1.3990 2.73E-01 2.73E-01
  1.5947 3.66E-01 3.66E-01
  1.7826 4.18E-01 4.18E-01
  1.9938 3.64E-01 3.64E-01
  2.2198 3.48E-01 3.48E-01
  2.4610 3.29E-01 3.29E-01
  2.6859 4.04E-01 4.04E-01
  2.8657 5.36E-01 5.36E-01
  3.0841 4.30E-01 4.30E-01
  3.3183 3.52E-01 3.52E-01
  3.4849 3.82E-01 3.82E-01
  3.7112 2.57E-01 2.57E-01
  3.9681 1.94E-01 1.94E-01
  4.1638 2.51E-01 2.51E-01
  4.3743 2.49E-01 2.49E-01
  4.5856 2.24E-01 2.24E-01
  4.7963 2.29E-01 2.29E-01
  5.0531 1.62E-01 1.62E-01
  5.2347 1.89E-01 1.89E-01
  5.4466 1.37E-01 1.37E-01
  5.6582 1.19E-01 1.19E-01
  5.8546 1.06E-01 1.06E-01
  6.0809 8.86E-02 8.86E-02
  6.2915 1.03E-01 1.03E-01
  6.5407 7.39E-02 7.39E-02
  6.7296 8.22E-02 8.22E-02
  7.1818 3.51E-02 3.51E-02
  7.3549 3.36E-02 3.36E-02
  7.6038 8.71E-02 8.71E-02
  7.8453 6.28E-02 6.28E-02
  8.0418 5.99E-02 5.99E-02
  8.2538 5.64E-02 5.64E-02
  8.4580 3.81E-02 3.81E-02
  8.6620 2.44E-02 2.44E-02
  8.8732 1.59E-02 1.59E-02
  9.1295 1.22E-02 1.22E-02
  9.3328 9.84E-03 9.84E-03
  9.5286 1.54E-02 1.54E-02
  9.7474 1.98E-02 1.98E-02
  9.9738 1.61E-02 1.61E-02
  10.208 1.25E-02 1.25E-02
  10.427 9.91E-03 9.91E-03
  10.593 7.55E-03 7.55E-03
  10.796 5.11E-03 5.11E-03
```

Appendix B. MCNP AmBe Model

MCNP Input Deck for Bare Setup Model

```
Input deck for Bare Scintillator - Based on Decker's thesis
c ******************************************************************
c Cell Cards
c ******************************************************************
100 3 -0.001225 -50 20 imp:n=1     $ Air in world (rpp)
200 2 -2.6989 -20 30 imp:n=1      $ Aluminum tube
300 0          -30 40 imp:n=1      $ Vacuum for the PMMA light pipe
400 1 -3.84     -40    imp:n=1      $ LiI(Eu) detector, modeled
500 4 -2.30    -10 50 imp:n=1      $ Concrete Walls
999 0           10     imp:n=0      $ Rest of the world (void)


c ******************************************************************
c Surface Cards
c ******************************************************************
10 RPP  -10 100 -50  50 0 100         $ Problem bounding surface - rectangular parallelpiped
20 RCC  30 0 49.2  0 0 1.6  0.635 $ Al right circular cylinder (perpendicular to beam)
30 RCC  30 0 49.4  0 0 1.2  0.535 $ Vacuum within the Al cylinder
40 RCC  30 0 49.8  0 0 0.4  0.2   $ LiI(Eu) crystal (RCC r=2mm, ht=4mm)
50 RPP  -5 95 -45 45 5 95            $ Concrete Walls Lining the problem bounding surface


c ******************************************************************
c Data Cards
c ******************************************************************
m1  03006.70c -0.0518  53127.70c -0.9482 $ LiI(Eu) crystal composition
m2  13027.70c -1.0000     $ Al metal
m3  7014.80c  -0.78    8016.80c  -0.22   $ Air
m4  1002   -0.022100
    6012   -0.002484
    8016   -0.574930
    11023  -0.015208
    12000  -0.001266
    13027  -0.019953
    14000  -0.304627
    19000  -0.010045
    20000  -0.042951
    26000  -0.006435 $ Concrete
mode n
SDEF POS=0.01 0 50 X=0 Y=d1 Z=d2            $ Source energy distribution
     PAR=n ERG=d3 VEC=1 0 0 DIR=1
SI1 -0.2 0.2
SP1 0 1
SI2 49.8 50.2
SP2 0 1
#   SI3 SP3
    0.0000     0.0000
    0.1067     0.1680
    0.3031     0.1577
    0.4998     0.1412
    0.7266     0.1253
    0.9685     0.1076
    1.1648     0.0997
    1.3990     0.0885
    1.5947     0.0973
    1.7826     0.1113
```

Continued

```
1.9938      0.1082
2.2198      0.1136
2.4610      0.1151
2.6859      0.1486
2.8657      0.1797
3.0841      0.1861
3.3183      0.1746
3.4849      0.1546
3.7112      0.1505
3.9681      0.1363
4.1638      0.1448
4.3743      0.1601
4.5856      0.1546
4.7963      0.1677
5.0531      0.1533
5.2347      0.1376
5.4466      0.1170
5.6582      0.1033
5.8546      0.0919
6.0809      0.0893
6.2915      0.1026
6.5407      0.0914
6.7296      0.0816
7.1818      0.0849
7.3549      0.0947
7.6038      0.0921
7.8453      0.0852
8.0418      0.0723
8.2538      0.0485
8.4580      0.0323
8.6620      0.0210
8.8732      0.0182
9.1295      0.0191
9.3328      0.0251
9.5286      0.0311
9.7474      0.0275
9.9738      0.0227
10.208      0.0180
10.427      0.0124
10.593      0.0067
10.796      0.0009
nps 300000                   $ Number of neutrons generated
F4:n 400                      $ Flux average tally in cell 400
E4 0.1067 49I 10.796
FM4 (1.4E-4 1 105)           $ FM tally multiplier for (n,t) reaction in m3       .
```

73

Appendix C. MCNP Response Function Model

MCNP input deck of 12 in Detector Setup Response Function

```
Input deck for Bare Scintillator - Based on Decker's thesis
c ********************************************************************
c Cell Cards
c ********************************************************************
100  0             -10 20   imp:n=1      $ Vacuum in world (rpp)
200  3  -0.95      -20 21   imp:n=1      $ Poly Bonner Sphere
210  3  -0.95      -21 22   imp:n=4
220  3  -0.95      -22 23   imp:n=13
230  3  -0.95      -23 24   imp:n=82
240  3  -0.95      -24 25   imp:n=405
250  3  -0.95      -25 30   imp:n=1500
300  2  -2.6989    -30 40   imp:n=12000 $ Aluminum tube
400  0             -40 50   imp:n=3000  $ Vacuum
500  1  -3.84      -50      imp:n=50000 $ LiI(Eu) detector, modeled
999  0              10      imp:n=0      $ Rest of the world (void)


c ********************************************************************
c Surface Cards
c ********************************************************************
10 RPP  0 100 -50  50 0 100          $ Problem bounding surface - rectangular parallelpiped
20 S     50 0 50   15.24             $ Polyethylene sphere - r in cm
21 S     50 0 50   12.7
22 S     50 0 50   10.15
23 S     50 0 50   6.35
24 S     50 0 50   3.81
25 S     50 0 50   2.54
30 RCC  49.2 0 50  1.6 0 0  0.725  $ Al right circular cylinder (perpendicular to beam)
40 RCC  49.4 0 50  1.2 0 0  0.525  $ Vacuum within the Al cylinder
50 RCC  49.8 0 50  0.4 0 0  0.2    $ LiI(Eu) crystal (RCC r=2mm, ht=4mm)


c ********************************************************************
c Data Cards
c ********************************************************************
m1  03006.70c -0.0518  53127.70c -0.9482  $ LiI(Eu) crystal composition
m2  13027.70c -1.0000                      $ Al metal
m3  01001.70c -0.143716 06012 -0.856284   $ Polyethylene
mode n
SDEF POS=0.01 0 50 AXS=1 0 0 RAD=d1 $ Source energy distribution
     PAR=n ERG=1.067E-01 VEC=1 0 0 DIR=1 ARA=729.65
SI1 0.0 15.24
SP1 -21 1
nps 300000          $ Number of neutrons generated
f4:n 500            $ Flux average tally in cell 500
MT3 poly.10t        $ S(a,B) treatment for hydrogen in polyethylene
FM4 (0.6386 1 105)  $ FM tally multiplier for (n,t) reaction in m3
```

Appendix D. MCNP Fat Man Model

MCNP input deck of the flat plain for 1 kT yield, 1 km HOB

```
Input deck for Bare Scintillator - Based on Decker's thesis
c ****************************************************************
c Cell Cards
c ****************************************************************
100  0              -10 20   imp:n=1      $ Vacuum in world (rpp)
200  3  -0.95       -20 21   imp:n=1      $ Poly Bonner Sphere
210  3  -0.95       -21 22   imp:n=4
220  3  -0.95       -22 23   imp:n=13
230  3  -0.95       -23 24   imp:n=82
240  3  -0.95       -24 25   imp:n=405
250  3  -0.95       -25 30   imp:n=1500
300  2  -2.6989     -30 40   imp:n=12000 $ Aluminum tube
400  0              -40 50   imp:n=3000  $ Vacuum
500  1  -3.84       -50      imp:n=50000 $ LiI(Eu) detector, modeled
999  0              10       imp:n=0     $ Rest of the world (void)


c ****************************************************************
c Surface Cards
c ****************************************************************
10 RPP  0 100 -50  50 0 100          $ Problem bounding surface - rectangular parallelpiped
20 S     50 0 50  15.24              $ Polyethylene sphere - r in cm
21 S     50 0 50  12.7
22 S     50 0 50  10.15
23 S     50 0 50  6.35
24 S     50 0 50  3.81
25 S     50 0 50  2.54
30 RCC  49.2 0 50  1.6 0 0  0.725  $ Al right circular cylinder (perpendicular to beam)
40 RCC  49.4 0 50  1.2 0 0  0.525  $ Vacuum within the Al cylinder
50 RCC  49.8 0 50  0.4 0 0  0.2    $ LiI(Eu) crystal (RCC r=2mm, ht=4mm)


c ****************************************************************
c Data Cards
c ****************************************************************
m1  03006.70c -0.0518  53127.70c -0.9482  $ LiI(Eu) crystal composition
m2  13027.70c -1.0000                      $ Al metal
m3  01001.70c -0.143716 06012 -0.856284    $ Polyethylene
mode n
SDEF POS=0.01 0 50 AXS=1 0 0 RAD=d1 $ Source energy distribution
     PAR=n ERG=1.067E-01 VEC=1 0 0 DIR=1 ARA=729.65
SI1 0.0 15.24
SP1 -21 1
nps 300000         $ Number of neutrons generated
f4:n 500           $ Flux average tally in cell 500
MT3 poly.10t       $ S(a,B) treatment for hydrogen in polyethylene
FM4 (0.6386 1 105) $ FM tally multiplier for (n,t) reaction in m3
```

Continued

```
This models the Fat Man with HOB of 1km.
c ************************************************************************
c  Cell Cards
c ************************************************************************
c Creating the cells for each of the surfaces (detector, the ground, air).
1 0           -100      imp:p,n=1                     $ Source
2 1 -0.001225 100 -200 imp:p,n=1.000006476516068     $ Air
3 2 -1.4       -300      imp:p,n=1.0000150453179792   $ Ground
4 0           -400 200:300 imp:p,n=0


c ************************************************************************
c Surfaces
c ************************************************************************
c Source Sphere (in cm)
100 SPH 0 0 1.0e+05 1.25892541e+00
c Rectangle Box (air)
200 BOX -1.05e+05 -1.05e+05 0
         2.10e+05 0 0
         0 2.10e+05 0
         0 0 2.05e+05
c Rectangle Box (ground)
300 BOX -1.05e+05 -1.05e+05 -1.05e+05
         2.10e+05 0 0
         0 2.10e+05 0
         0 0 1.05e+05
c Boundary cube that is void.
400 BOX -1.051e+05 -1.051e+05 -1.051e+05
         2.102e+05 0 0
         0 2.102e+05 0
         0 0 2.102e+05


c ********************************************************************
c Data Cards
c ********************************************************************
xs1 7014.00c 13.882780 7014.800nc 0 1 3 190999 0 0 2.5301e-08 $ N14_ENDF8
phys:n
phys:p 3J -1
mode p n
c -------------- Materials ---------------
m1 7014.80c 1.0 gas=1  $ Nitrogen, density = 0.001225 g/cm3
m2 8016.80c -0.5 14028.80c -0.3 13027.80c -0.1 26054.80c -0.1  $ Ground, density = 1.4 g/cm3
c -------------- Sources ---------------
c This says that the source is a point source located at (0,0,1e) with n energy = 14 MeV.
SDEF pos 0 0 1.0e+05 erg=d1 par=n wgt=1.590e23
c Fat Man Neutron Spectrum
```

Continued

```
c White, Whalen and Heath 2001
c LA-UR-01-6594
c Optional Weighting (per kT): wgt=1.590e23
#    sil spl
     1.00000e-11 0.00000e+00
     5.00000e-10 0.00000e+00
     2.00000e-09 0.00000e+00
     5.00000e-09 0.00000e+00
     1.00000e-08 0.00000e+00
     1.45000e-08 0.00000e+00
     2.10000e-08 7.11092e+15
     3.00000e-08 1.49022e+16
     4.00000e-08 1.84908e+16
     5.00000e-08 3.58135e+16
     7.00000e-08 1.53297e+17
     1.00000e-07 2.79198e+17
     1.25000e-07 3.43142e+17
     1.50000e-07 4.79701e+17
     1.84000e-07 4.89034e+17
     2.25000e-07 1.13498e+18
     2.75000e-07 1.32765e+18
     3.25000e-07 1.78285e+18
     3.67000e-07 1.90508e+18
     4.14000e-07 1.82319e+18
     5.00000e-07 4.19008e+18
     5.32000e-07 1.89725e+18
     6.25000e-07 5.63274e+18
     6.83000e-07 3.82641e+18
     8.00000e-07 9.76020e+18
     8.76000e-07 7.30359e+18
     1.00000e-06 1.26865e+19
     1.04000e-06 4.18286e+18
     1.08000e-06 4.74523e+18
     1.13000e-06 4.95536e+18
     1.30000e-06 2.30066e+19
     1.45000e-06 2.05259e+19
     1.86000e-06 6.68944e+19
     2.38000e-06 1.07537e+20
     3.06000e-06 1.67206e+20
     3.93000e-06 2.67818e+20
     5.04000e-06 4.15215e+20
     6.48000e-06 6.44258e+20
     8.32000e-06 9.81439e+20
     1.07000e-05 1.47878e+21
     1.37000e-05 2.17362e+21
```

Continued

```
1.76000e-05 3.12796e+21
2.26000e-05 4.35325e+21
2.90000e-05 5.87599e+21
3.73000e-05 7.62271e+21
4.79000e-05 9.46517e+21
6.14000e-05 1.11511e+22
7.89000e-05 1.25419e+22
1.01000e-04 1.34331e+22
1.30000e-04 1.37763e+22
1.67000e-04 1.36920e+22
2.14000e-04 1.31742e+22
2.75000e-04 1.22529e+22
3.54000e-04 1.07416e+22
4.54000e-04 8.54996e+21
5.83000e-04 5.81036e+21
7.49000e-04 3.32485e+21
9.61000e-04 1.58475e+21
1.23000e-03 6.32215e+20
1.58000e-03 2.15616e+20
2.03000e-03 6.12346e+19
2.25000e-03 1.00131e+19
2.49000e-03 8.75468e+18
2.61000e-03 3.39771e+18
2.75000e-03 2.51682e+18
3.04000e-03 5.81036e+18
3.35000e-03 4.85301e+18
3.71000e-03 4.61096e+18
4.31000e-03 6.05120e+18
5.53000e-03 1.02961e+19
7.10000e-03 1.02359e+19
9.12000e-03 1.04346e+19
1.06000e-02 6.00665e+18
1.17000e-02 3.59640e+18
1.50000e-02 1.04647e+19
1.93000e-02 1.17411e+19
2.19000e-02 6.48472e+18
2.36000e-02 4.54292e+18
2.42000e-02 1.62750e+18
2.48000e-02 1.60583e+18
2.61000e-02 3.72646e+18
2.70000e-02 2.77091e+18
2.85000e-02 1.08560e+18
3.18000e-02 2.84617e+18
3.43000e-02 1.95866e+18
4.09000e-02 4.45140e+18
```

Continued

```
4.63000e-02  6.29205e+18
5.25000e-02  6.53289e+18
5.66000e-02  4.07207e+18
6.74000e-02  1.16388e+19
7.20000e-02  6.04518e+18
7.95000e-02  7.69496e+18
8.25000e-02  2.35485e+18
8.65000e-02  1.44266e+18
9.80000e-02  6.14152e+18
1.11000e-01  9.07982e+18
1.17000e-01  4.57122e+18
1.23000e-01  3.63855e+18
1.29000e-01  5.87117e+18
1.36000e-01  5.74052e+18
1.43000e-01  3.49766e+18
1.50000e-01  2.70167e+18
1.58000e-01  3.29354e+18
1.66000e-01  3.94924e+18
1.74000e-01  4.81086e+18
1.83000e-01  5.57674e+18
1.93000e-01  5.17995e+18
2.02000e-01  4.20333e+18
2.13000e-01  4.01427e+18
2.24000e-01  4.88070e+18
2.35000e-01  5.43645e+18
2.47000e-01  6.40645e+18
2.73000e-01  1.42519e+19
2.87000e-01  5.92717e+18
2.95000e-01  3.19540e+18
2.97000e-01  1.32946e+18
2.98000e-01  4.63926e+17
3.02000e-01  1.54200e+18
3.34000e-01  1.32585e+19
3.69000e-01  1.57693e+19
3.88000e-01  6.88814e+18
4.08000e-01  7.91775e+18
4.50000e-01  1.12354e+19
4.98000e-01  1.77201e+19
5.23000e-01  1.01335e+19
5.50000e-01  1.08079e+19
5.78000e-01  1.14040e+19
6.08000e-01  1.41135e+19
6.39000e-01  1.32163e+19
6.72000e-01  1.32163e+19
7.07000e-01  1.34451e+19
```

Continued

```
7.43000e-01 1.44868e+19
7.81000e-01 1.39027e+19
8.21000e-01 1.30116e+19
8.63000e-01 1.39810e+19
9.07000e-01 1.32645e+19
9.62000e-01 1.58957e+19
1.00000e+00 9.09186e+18
1.11000e+00 2.46444e+19
1.16000e+00 1.60041e+19
1.22000e+00 1.67447e+19
1.29000e+00 1.76719e+19
1.35000e+00 1.55465e+19
1.42000e+00 1.86052e+19
1.50000e+00 1.96890e+19
1.57000e+00 1.92495e+19
1.65000e+00 1.82319e+19
1.74000e+00 2.11642e+19
1.83000e+00 2.00442e+19
1.92000e+00 1.89845e+19
2.02000e+00 2.00984e+19
2.12000e+00 2.18506e+19
2.23000e+00 2.31933e+19
2.31000e+00 1.68350e+19
2.35000e+00 1.05249e+19
2.37000e+00 5.08662e+18
2.39000e+00 5.32927e+18
2.47000e+00 1.76719e+19
2.59000e+00 2.12244e+19
2.73000e+00 2.08029e+19
2.87000e+00 1.91230e+19
3.01000e+00 1.62329e+19
3.17000e+00 1.70397e+19
3.33000e+00 1.13618e+19
3.68000e+00 2.04597e+19
4.07000e+00 2.17422e+19
4.49000e+00 2.19349e+19
4.72000e+00 1.39328e+19
4.97000e+00 1.38365e+19
5.23000e+00 1.22770e+19
5.49000e+00 1.01576e+19
5.77000e+00 9.01359e+18
6.07000e+00 8.99552e+18
6.37000e+00 7.33972e+18
6.59000e+00 4.48933e+18
6.70000e+00 2.12244e+18
```

Continued

```
          6.37000e+00 7.33972e+18
          6.59000e+00 4.48933e+18
          6.70000e+00 2.12244e+18
          7.05000e+00 6.28001e+18
          7.41000e+00 3.89625e+18
          7.79000e+00 2.87688e+18
          8.19000e+00 2.20613e+18
          8.61000e+00 2.57282e+18
          9.05000e+00 1.82921e+18
          9.51000e+00 1.62148e+18
          1.00000e+01 9.32066e+17
          1.05000e+01 6.38236e+17
          1.11000e+01 5.66525e+17
          1.16000e+01 4.41046e+17
          1.22000e+01 3.29113e+17
          1.25000e+01 6.84599e+16
          1.28000e+01 7.95989e+16
          1.35000e+01 7.79732e+16
          1.38000e+01 1.66604e+16
          1.42000e+01 4.25330e+16
          1.46000e+01 3.52054e+16
          1.49000e+01 5.38527e+16
          1.57000e+01 4.81567e+16
          1.65000e+01 1.50648e+16
          1.69000e+01 1.65460e+16
          1.73000e+01 0.00000e+00
          1.96000e+01 3.97091e+16
c --------------- Tallies ---------------
fc15 n Flux (particles/cm2) for a point detector
f15:n 1.0e+05 0 5e+02 1e+02
e15 1e-08 98ilog 20 NT
fc25 p Flux for a point detector
f25:p 1.0e+05 0 5e+02 1e+02
e25 1e-08 98ilog 20 NT
rand gen 2 seed 42050674584365 stride 2000000
nps 1000000
```

MCNP input deck of a single building on a flat plain for 1 kT yield, 1 km HOB

```
This models the Fat Man with HOB of 1km.
c ***********************************************************************
c   Cell Cards
c ***********************************************************************
c Creating the cells for each of the surfaces (detector, the ground, air).
1 0            -100     imp:p,n=1                     $ Source
2 1 -0.001225 -200 400 (100) imp:p,n=1.000006476516068   $ Air
3 2 -1.4       -300     imp:p,n=1.0000150453179792  $ Ground
4 3 -2.30      -400 500 imp:p,n=1.0000322509752055  $ Concrete Walls/floor/ceiling of building
5 1 -0.001225 -500      imp:p,n=1.00006469211132041 $ Air inside building
6 0            -600 200:300 imp:p,n=0

c ***********************************************************************
c Surfaces
c ***********************************************************************
c Source Sphere (in cm)
100 SPH 0 0 1.0e+05 1.25892541e+00
c Rectangle Box (air)
200 BOX -1.05e+05 -1.05e+05 0
        2.10e+05 0 0
        0 2.10e+05 0
        0 0 2.05e+05
c Rectangle Box (ground)
300 BOX -1.05e+05 -1.05e+05 -1.05e+05
        2.10e+05 0 0
        0 2.10e+05 0
        0 0 1.05e+05
c 100 m Tall Building Outer Box centered on origin
400 BOX -1.00e+03 -1.00e+03 0
        2.00e+03 0 0
        0 2.00e+03 0
        0 0 1.00e+04
c 100 m Tall Building Inner box
500 BOX -9.00e+02 -9.00e+02 1.00e+02
        1.80e+03 0 0
        0 1.80e+03 0
        0 0 9.80e+03
c Boundary cube that is void.
600 BOX -1.051e+05 -1.051e+05 -1.051e+05
        2.102e+05 0 0
        0 2.102e+05 0
        0 0 2.102e+05

c ***********************************************************************
c Data Cards
```

Continued

```
c **************************************************************
phys:n
phys:p 3J -1
mode p n
c --------------- Materials ---------------
m1 7014.80c 1.0 gas=1  $ Nitrogen, density = 0.001225 g/cm3
m2 8016.80c -0.5 14028.80c -0.3 13027.80c -0.1 26054.80c -0.1  $ Ground, censity = 1.4 g/cm3
m3 1002   -0.022100
   6012   -0.002484
   8016   -0.574930
   11023  -0.015208
   12000  -0.001266
   13027  -0.019953
   14000  -0.304627
   19000  -0.010045
   20000  -0.042951
   26000  -0.006435 $ Concrete
c --------------- Sources ---------------
c Point source - 1kT - 1km HOB.
SDEF pos 0 0 1.0e+05 erg=d1 par=n wgt=1.590e23
c Fat Man Neutron Spectrum
c White, Whalen and Heath 2001
c LA-UR-01-6594
c Optional Weighting (per kT): wgt=1.590e23
#    si1 sp1
     1.00000e-11 0.00000e+00
     5.00000e-10 0.00000e+00
     2.00000e-09 0.00000e+00
     5.00000e-09 0.00000e+00
     1.00000e-08 0.00000e+00
     1.45000e-08 0.00000e+00
     2.10000e-08 7.11092e+15
     3.00000e-08 1.49022e+16
     4.00000e-08 1.84908e+16
     5.00000e-08 3.58135e+16
     7.00000e-08 1.53297e+17
     1.00000e-07 2.79198e+17
     1.25000e-07 3.43142e+17
     1.50000e-07 4.79701e+17
     1.84000e-07 4.89034e+17
     2.25000e-07 1.13498e+18
     2.75000e-07 1.32765e+18
     3.25000e-07 1.78285e+18
     3.67000e-07 1.90508e+18
     4.14000e-07 1.82319e+18
```

Continued

```
5.00000e-07 4.19008e+18
5.32000e-07 1.89725e+18
6.25000e-07 5.63274e+18
6.83000e-07 3.82641e+18
8.00000e-07 9.76020e+18
8.76000e-07 7.30359e+18
1.00000e-06 1.26865e+19
1.04000e-06 4.18286e+18
1.08000e-06 4.74523e+18
1.13000e-06 4.95536e+18
1.30000e-06 2.30066e+19
1.45000e-06 2.05259e+19
1.86000e-06 6.68944e+19
2.38000e-06 1.07537e+20
3.06000e-06 1.67206e+20
3.93000e-06 2.67818e+20
5.04000e-06 4.15215e+20
6.48000e-06 6.44258e+20
8.32000e-06 9.81439e+20
1.07000e-05 1.47878e+21
1.37000e-05 2.17362e+21
1.76000e-05 3.12796e+21
2.26000e-05 4.35325e+21
2.90000e-05 5.87599e+21
3.73000e-05 7.62271e+21
4.79000e-05 9.46517e+21
6.14000e-05 1.11511e+22
7.89000e-05 1.25419e+22
1.01000e-04 1.34331e+22
1.30000e-04 1.37763e+22
1.67000e-04 1.36920e+22
2.14000e-04 1.31742e+22
2.75000e-04 1.22529e+22
3.54000e-04 1.07416e+22
4.54000e-04 8.54996e+21
5.83000e-04 5.81036e+21
7.49000e-04 3.32485e+21
9.61000e-04 1.58475e+21
1.23000e-03 6.32215e+20
1.58000e-03 2.15616e+20
2.03000e-03 6.12346e+19
2.25000e-03 1.00131e+19
2.49000e-03 8.75468e+18
2.61000e-03 3.39771e+18
2.75000e-03 2.51682e+18
```

Continued

```
3.04000e-03 5.81036e+18
3.35000e-03 4.85301e+18
3.71000e-03 4.61096e+18
4.31000e-03 6.05120e+18
5.53000e-03 1.02961e+19
7.10000e-03 1.02359e+19
9.12000e-03 1.04346e+19
1.06000e-02 6.00665e+18
1.17000e-02 3.59640e+18
1.50000e-02 1.04647e+19
1.93000e-02 1.17411e+19
2.19000e-02 6.48472e+18
2.36000e-02 4.54292e+18
2.42000e-02 1.62750e+18
2.48000e-02 1.60583e+18
2.61000e-02 3.72646e+18
2.70000e-02 2.77091e+18
2.85000e-02 1.08560e+18
3.18000e-02 2.84617e+18
3.43000e-02 1.95866e+18
4.09000e-02 4.45140e+18
4.63000e-02 6.29205e+18
5.25000e-02 6.53289e+18
5.66000e-02 4.07207e+18
6.74000e-02 1.16388e+19
7.20000e-02 6.04518e+18
7.95000e-02 7.69496e+18
8.25000e-02 2.35485e+18
8.65000e-02 1.44266e+18
9.80000e-02 6.14152e+18
1.11000e-01 9.07982e+18
1.17000e-01 4.57122e+18
1.23000e-01 3.63855e+18
1.29000e-01 5.87117e+18
1.36000e-01 5.74052e+18
1.43000e-01 3.49766e+18
1.50000e-01 2.70167e+18
1.58000e-01 3.29354e+18
1.66000e-01 3.94924e+18
1.74000e-01 4.81086e+18
1.83000e-01 5.57674e+18
1.93000e-01 5.17995e+18
2.02000e-01 4.20333e+18
2.13000e-01 4.01427e+18
2.24000e-01 4.88070e+18
```

Continued

```
2.35000e-01 5.43645e+18
2.47000e-01 6.40645e+18
2.73000e-01 1.42519e+19
2.87000e-01 5.92717e+18
2.95000e-01 3.19540e+18
2.97000e-01 1.32946e+18
2.98000e-01 4.63926e+17
3.02000e-01 1.54200e+18
3.34000e-01 1.32585e+19
3.69000e-01 1.57693e+19
3.88000e-01 6.88814e+18
4.08000e-01 7.91775e+18
4.50000e-01 1.12354e+19
4.98000e-01 1.77201e+19
5.23000e-01 1.01335e+19
5.50000e-01 1.08079e+19
5.78000e-01 1.14040e+19
6.08000e-01 1.41135e+19
6.39000e-01 1.32163e+19
6.72000e-01 1.32163e+19
7.07000e-01 1.34451e+19
7.43000e-01 1.44868e+19
7.81000e-01 1.39027e+19
8.21000e-01 1.30116e+19
8.63000e-01 1.39810e+19
9.07000e-01 1.32645e+19
9.62000e-01 1.58957e+19
1.00000e+00 9.09186e+18
1.11000e+00 2.46444e+19
1.16000e+00 1.60041e+19
1.22000e+00 1.67447e+19
1.29000e+00 1.76719e+19
1.35000e+00 1.55465e+19
1.42000e+00 1.86052e+19
1.50000e+00 1.96890e+19
1.57000e+00 1.92495e+19
1.65000e+00 1.82319e+19
1.74000e+00 2.11642e+19
1.83000e+00 2.00442e+19
1.92000e+00 1.89845e+19
2.02000e+00 2.00984e+19
2.12000e+00 2.18506e+19
2.23000e+00 2.31933e+19
2.31000e+00 1.68350e+19
2.35000e+00 1.05249e+19
```

Continued

```
2.37000e+00 5.08662e+18
2.39000e+00 5.32927e+18
2.47000e+00 1.76719e+19
2.59000e+00 2.12244e+19
2.73000e+00 2.08029e+19
2.87000e+00 1.91230e+19
3.01000e+00 1.62329e+19
3.17000e+00 1.70397e+19
3.33000e+00 1.13618e+19
3.68000e+00 2.04597e+19
4.07000e+00 2.17422e+19
4.49000e+00 2.19349e+19
4.72000e+00 1.39328e+19
4.97000e+00 1.38365e+19
5.23000e+00 1.22770e+19
5.49000e+00 1.01576e+19
5.77000e+00 9.01359e+18
6.07000e+00 8.99552e+18
6.37000e+00 7.33972e+18
6.59000e+00 4.48933e+18
6.70000e+00 2.12244e+18
7.05000e+00 6.28001e+18
7.41000e+00 3.89625e+18
7.79000e+00 2.87688e+18
8.19000e+00 2.20613e+18
8.61000e+00 2.57282e+18
9.05000e+00 1.82921e+18
9.51000e+00 1.62148e+18
1.00000e+01 9.32066e+17
1.05000e+01 6.38236e+17
1.11000e+01 5.66525e+17
1.16000e+01 4.41046e+17
1.22000e+01 3.29113e+17
1.25000e+01 6.84599e+16
1.28000e+01 7.95989e+16
1.35000e+01 7.79732e+16
1.38000e+01 1.66604e+16
1.42000e+01 4.25330e+16
1.46000e+01 3.52054e+16
1.49000e+01 5.38527e+16
1.57000e+01 4.81567e+16
1.65000e+01 1.50648e+16
1.69000e+01 1.65460e+16
1.73000e+01 0.00000e+00
1.96000e+01 3.97091e+16
```

Continued

```
c --------------- Tallies ---------------
fc15 n Flux (particles/cm2) for a point detector
f15:n 1.0e+05 0 5e+02 1e+02
e15 1e-08 98ilog 20 NT
fc25 p Flux for a point detector
f25:p 1.0e+05 0 5e+02 1e+02
e25 1e-08 98ilog 20 NT
rand gen 2 seed 42050674584365 stride 2000000
nps 1000000
```

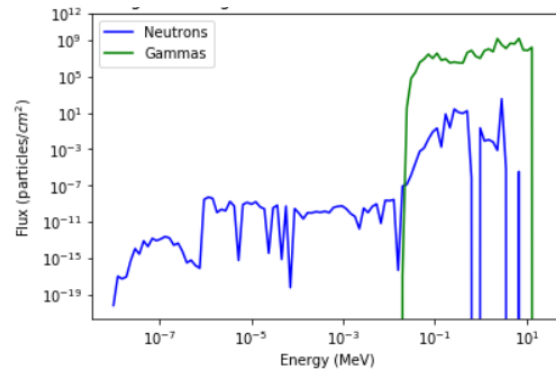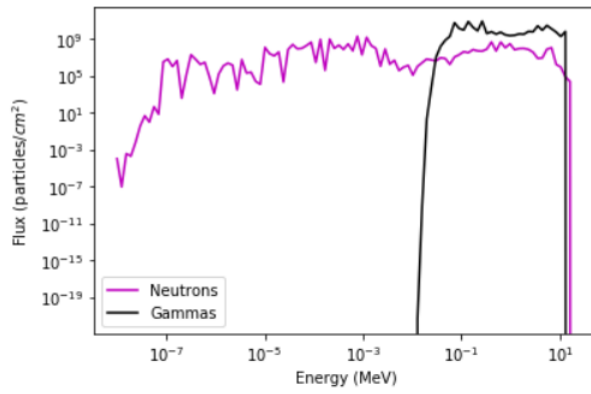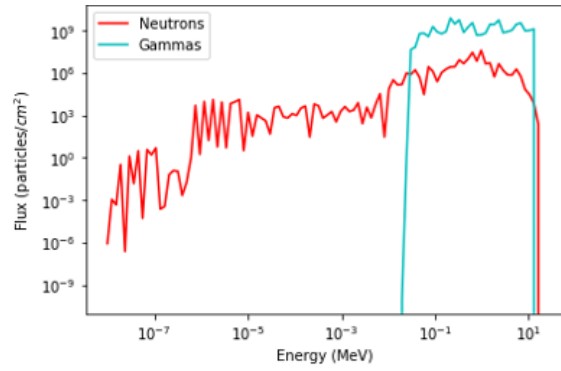Plots for the flat plain model for 10 kT yield, for HOBs 1 km, 200 m, and 10 m, respectfully
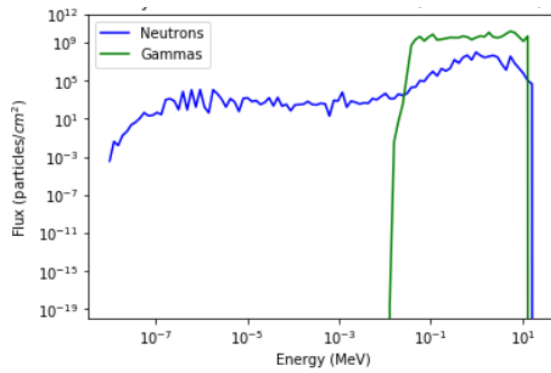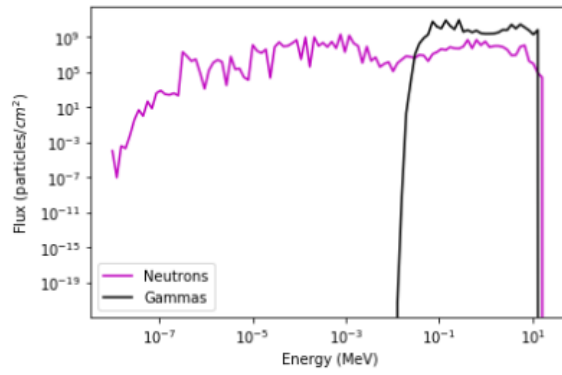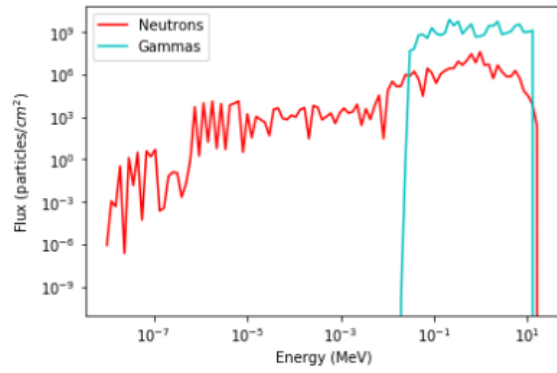
Plots for the flat plain model for 100 kT yield, for HOBs 1 km, 200 m, and 10 m, respectfully
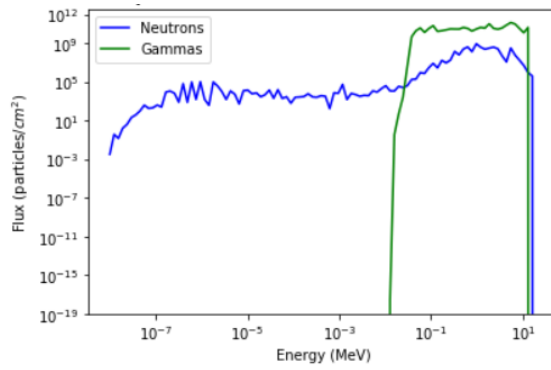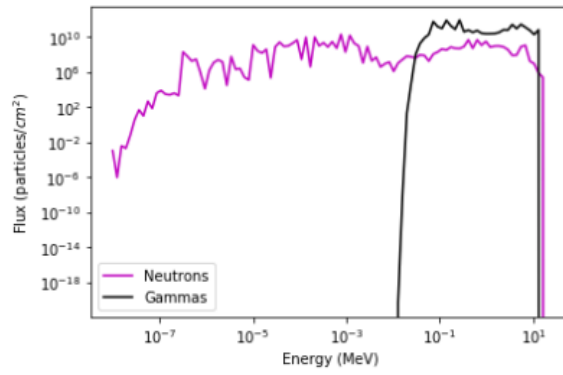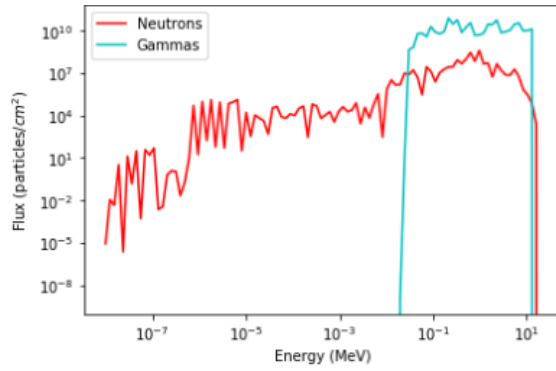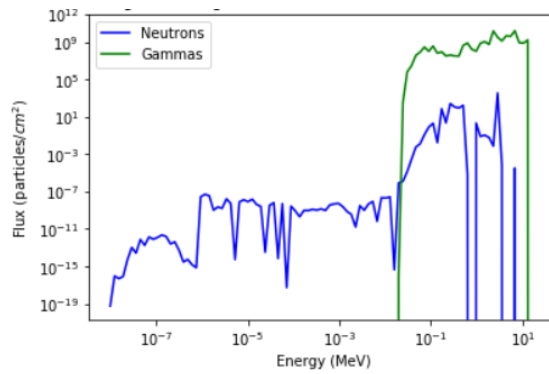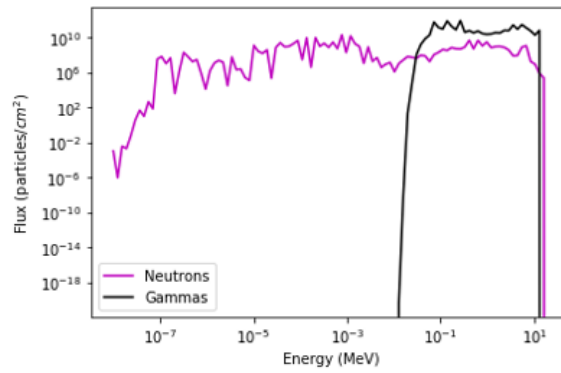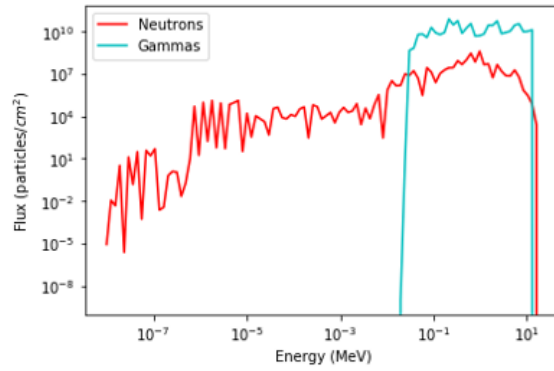
Plots for the single building on a flat plain model for 10 kT yield, for HOBs 1 km, 200 m, and 10 m, respectfully

Plots for the single building on a flat plain model for 100 kT yield, for HOBs 1 km, 200 m, and 10 m, respectfully

Bibliography

1. D. Culver and Y. Seo, "North Korea testing 'creative' weapons that could threaten US, experts say," Article, Sept 2019. [Online]. Available: https://www.cnn.com/2019/09/08/asia/north-korea-weapons-tests-intl-hnk/index.html

2. "2018 Nuclear Posture Review," Article. [Online]. Available: https://media.defense.gov/2018/Feb/02/2001872888/-1/-1/1/2018-NUCLEAR-POSTURE-REVIEW.PDF

3. R. Stone, "Surprise nuclear strike? Here's how we'll figure out who did it," Article, Mar 2016. [Online]. Available: https://www.sciencemag.org/news/2016/03/surprise-nuclear-strike-heres-how-well-figure-out-who-did-it

4. D. L. R. Cao, "Solar panel for prompt detection and identification of nuclear detonations," Presentation.

5. *Ludlum Model 42-5 Neutron Ball Cart*, Ludlum Measurements, Inc., Aug 2015, accessed: 02-15-2020.

6. P. Goldhagen, *HASL-300: EML Procedures Manual, 28th Edition*, Nuclear Waste Partnership LLC., Feb 1997, accessed: 02-15-2020.

7. K. S. Krane, *Introductory Nuclear Physics.* John Wiley Sons, Inc., 1988.

8. G. F. Knoll, *Radiation Detection and Measurement*, 3rd ed. John Wiley and Sons, Inc., 2000.

9. "Introduction to Reaction Rates," Presentation. [Online]. Available: http://users.jyu.fi/~ajokinen/FYSN440/FYSN440_Lecture3.pdf

10. "For chemical analysis: Neutron Activation Analysis," Online, Integrated Infrastructure Initiative for Neutron Scattering and Muon Spectroscopy (NMI3), Tech. Rep., 2012, accessed: 2-11-2020. [Online]. Available: https://nmi3.eu/neutron-research/techniques-for-/chemical-analysis.html

11. D. S. Leoni, "Interaction of Neutrons with Matter," Presentation. [Online]. Available: http://www0.mi.infn.it/~sleoni/TEACHING/Nuc-Phys-Det/PDF/Lezione-partI-3-neutrons.pdf

12. "Neutron Interactions and Applications: Brief Introduction to Transport Theory/Monte Carlo Techniques/MCNP," PDF. [Online]. Available: http://web.mit.edu/22.54/ClassNotes/Lec2.pdf

13. I. Lux and L. Koblinger, *Monte Carlo Particle Transport Methods: Neutron and Photon Calculations.* CRC Press, 1991.

14. *MCNP6 User's Manual Version 1.0*, Los Alamos National Security, LLC, May 2013, accessed: 12-23-2019.

15. "Neutron Detection: Neutron Interactions and Applications," Presentation, 2010.

16. S. Masciocchi, "Semiconductor Detectors," Presentation, Oct 2017. [Online]. Available: https://www.physi.uni-heidelberg.de/~sma/teaching/ GraduateDays2017/sma_Detectors_3_Semiconductors.pdf

17. S. Harrison, "Semiconductor-Based Thermal Neutron Detectors," Article, Feb 2013. [Online]. Available: http://large.stanford.edu/courses/2013/ph241/ harrison1/

18. "Scintillation Counter – Scintillation Detector," Article, 2020. [Online]. Available: https://www.nuclear-power.net/nuclear-engineering/radiation-detection/ scintillation-counter-scintillation-detector/

19. "Evaluated Nuclear Data File (ENDF) Database," Jan.

20. S. Mukhopadhyay and H. McHugh, "Portable gamma and thermal neutron detector using LiI(Eu) crystals," Online, Remote Sensing Laboratory, Special Technology Laboratories, Tech. Rep., accessed: 12-28-2019. [Online]. Available: https://www.osti.gov/servlets/purl/811395

21. "Neutron Moderators," Article. [Online]. Available: https://www.radioactivity. eu.com/site/pages/Neutrons_Moderators.htm

22. "Solid Scintillators," Presentation, Jan 2010. [Online]. Available: https: //www.nrc.gov/docs/ML1122/ML11229A680.pdf

23. A. W. Decker, "Verification and validation of monte carlo n-particle code 6 (mcnp6) with neutron protection factor measurements of an iron box," Master's thesis, Air Force Institute of Technology, Mar 2014, accessed: 10/12/2019.

24. R. Holmes, *Gamma ray and neutron sources (AAEC/S–24)*. International Nuclear Information System, 1982.

25. *Neutron Flux*, United State Nuclear Regulatory Commission, Mar 2019, accessed: 02-15-2020.

26. M. Reginatto and P. Goldhagen, *MAXED, A Computer Code For The Deconvolution Of Multisphere Neutron Spectrometer Data Using The Maximum Entropy Method*, Environmental Measurements Laboratory, June 1998, accessed: 12-23-2019.

27. M. Reginatto, *The "few-channel" unfolding programs in the UMG package: MXD_FC33, GRV_FC33 and IGU_FC33*, Physikalisch-Technische Bundesanstalt (PTB), March 2004, accessed: 12-23-2019.

28. "ISO 8529-1:2001(en) Reference neutron radiations," Online, International Organization for Standardization, Tech. Rep., 2001, accessed: 1-8-2020. [Online]. Available: https://www.iso.org/obp/ui/#iso:std:iso:8529:-1:ed-1:v1:en

29. "Gamma Energy (keV)," PDF, Sept 2015. [Online]. Available: https://physics.indiana.edu/~courses/p451/examples/Gamma_Energies_table.pdf

REPORT DOCUMENTATION PAGE

Form Approved
OMB No. 0704–0188

The public reporting burden for this collection of information is estimated to average 1 hour per response, including the time for reviewing instructions, searching existing data sources, gathering and maintaining the data needed, and completing and reviewing the collection of information. Send comments regarding this burden estimate or any other aspect of this collection of information, including suggestions for reducing this burden to Department of Defense, Washington Headquarters Services, Directorate for Information Operations and Reports (0704–0188), 1215 Jefferson Davis Highway, Suite 1204, Arlington, VA 22202–4302. Respondents should be aware that notwithstanding any other provision of law, no person shall be subject to any penalty for failing to comply with a collection of information if it does not display a currently valid OMB control number. **PLEASE DO NOT RETURN YOUR FORM TO THE ABOVE ADDRESS.**

1. REPORT DATE *(DD–MM–YYYY)*	2. REPORT TYPE	3. DATES COVERED *(From — To)*
26-03-2020	Master's Thesis	October 2019 — March 2020

4. TITLE AND SUBTITLE

Determination and Simulation of the Neutron Spectrum of Nuclear Detonations and Surrogate Sources

5a. CONTRACT NUMBER

5b. GRANT NUMBER

5c. PROGRAM ELEMENT NUMBER

6. AUTHOR(S)

Nichols, Taylor M., Contractor, USAF

5d. PROJECT NUMBER

20ENP

5e. TASK NUMBER

5f. WORK UNIT NUMBER

7. PERFORMING ORGANIZATION NAME(S) AND ADDRESS(ES)

Air Force Institute of Technology
Graduate School of Engineering and Management (AFIT/ENP)
2950 Hobson Way
WPAFB OH 45433-7765

8. PERFORMING ORGANIZATION REPORT NUMBER

AFIT-ENP-MS-20-M-109

9. SPONSORING / MONITORING AGENCY NAME(S) AND ADDRESS(ES)

Defense Threat Reduction Agency-RD-NT
Dr. David Petersen
8725 John J. Kingman Rd.
Ft. Belvoir, VA 22060
david.c.petersen16.civ@mail.mil

10. SPONSOR/MONITOR'S ACRONYM(S)

DTRA-RD

11. SPONSOR/MONITOR'S REPORT NUMBER(S)

12. DISTRIBUTION / AVAILABILITY STATEMENT

DISTRIBUTION STATEMENT A:
APPROVED FOR PUBLIC RELEASE; DISTRIBUTION UNLIMITED.

13. SUPPLEMENTARY NOTES

14. ABSTRACT

This research determined a methodology for characterizing the Fast Beam Facility (FBF) at The Ohio State University Nuclear Reactor Laboratory to test the response of photovoltaic arrays to nuclear weapon radiation. Additionally, this research developed neutron and gamma nuclear weapon output spectra of two environments for comparison to the FBF spectrum. A Bonner sphere spectrometer (BSS), coupled with the unfolding program Maximum Entropy Deconvolution (MAXED), was employed as a means of determining the energy spectrum of neutrons. Using the ISO 8529 americium beryllium (AmBe) source as the a priori default spectrum, MAXED was used to unfold the spectrum of neutrons detected using the BSS from a 500 mCi AmBe source. An MCNP model of the experiment was created with the ISO 8529 spectrum used as the neutron source spectrum. The resulting unfolded neutron spectrum has similar characteristics to the ISO 8529 reference spectrum, with peaks located at 3.1 and 4.7 MeV corresponding to the peaks of the reference spectrum. Spectral deviations from the ISO 8529 reference spectrum caused by low-energy, non-neutron interaction events or neutrons thermalized through interactions in the experimental environment are accounted for in the model and reflected in the final unfolded neutron spectrum. Next, the neutron and gamma flux received at a fixed photovoltaic array from two detonation scenarios were modeled with MCNP6: a ground-only and a single building model for various height-of-bursts and yields. Thermalization due to neutron interaction and scattering of gamma rays with environmental materials is observed in the spectrum of resulting radiation incident on the photovoltaic array.

15. SUBJECT TERMS

Neutron Detection, Nuclear Weapon Radiation, Neutron Transport

16. SECURITY CLASSIFICATION OF:			17. LIMITATION OF ABSTRACT	18. NUMBER OF PAGES	19a. NAME OF RESPONSIBLE PERSON
a. REPORT	b. ABSTRACT	c. THIS PAGE			Dr. John McClory, AFIT/ENP
U	U	U	U	109	19b. TELEPHONE NUMBER *(include area code)* (937) 255-3636, x7308; john.mcclory@afit.edu

Standard Form 298 (Rev. 8–98)
Prescribed by ANSI Std. Z39.18